



Milad Khosravi · Mitra Javan

Three-dimensional flow structure and mixing of the side thermal buoyant jet discharge in cross-flow

Received: 26 November 2019 / Revised: 17 March 2020 / Published online: 28 June 2020
© Springer-Verlag GmbH Austria, part of Springer Nature 2020

Abstract Numerical investigation of a side thermal buoyant discharge in the cross-flow is presented based on unsteady Reynolds-averaged Navier–Stokes equations closed with the realizable k - ε turbulence model. Emphasis is placed on the detailed three-dimensional flow evolution and scalar mixing in an incompressible turbulent environment. The present study covers the cases with different jets to cross-flow velocity ratios (R) and initial temperatures. Moreover, various flow characteristics, including vortical structures, jet trajectories, jet streamlines, and intrinsic instabilities, are examined. Mixing ability is quantified by the decay rate of scalar temperatures and velocity magnitude, the probability density function, the spatial mixing deficiencies (SMDs), power spectral density analysis, and temporal mixing deficiencies (TMDs). Comparing the simulation results with the experimental data of Abdelwahed (Surface jets and surface plumes in cross-flows. Ph.D. thesis, Department of Civil Engineering and Applied Mechanics, McGill University, Montreal, Quebec, 1981), it shows good agreement in terms of the temperature half-width and half-thickness profiles, recirculation zone size, and jet trajectory. The numerical results of three-dimensional structures indicate a shear-layer, horseshoe, and surface roller vortices near the side-channel exit and secondary flows after the recirculation zone at the free surface of the main channel. The instantaneous temperature contours exhibit a vortex shedding phenomenon and gaps between the cross-flow and discharge jet at the shear layer. The maximum velocity magnitude location approaches the outer wall toward the main-channel downstream by increasing R . It is found that as the densimetric Froude number (Fr_0) and R increase, the temperature dilution (S) generally decreases. The statistical analysis of TMD and SMD indicates a direct relationship between the mixing efficiency and buoyancy flux (F_0).

Keywords Numerical investigation · Thermal buoyant discharge · Flow evolution · Scalar mixing · Three-dimensional structures

List of symbols

\bar{T}	Temperature (K)
T_k	Reference temperature
T_a	Temperature in the cross-flow inlet
T_0	Difference in temperature between the jet and cross-flow
T	Time-averaged excess temperature
T_m	Maximum time-averaged excess temperature
T_s	Temperature scale
t	Time

α	Probability calculated by PDF
ξ	Statistical representation of α
l_s	Length scale (m)
t_s	Time scale (s)
$2\eta_m$	T_m Half-width (m)
M_0	Flow force in the side-channel inlet (m^4/s^2)
F_0	Buoyancy flux in the side-channel inlet (m^4/s^3)
Γ_0	Heat flux in the side-channel inlet (km^3/s)
δ_{ij}	Kronecker delta function
ν_0	Kinematic viscosity (m^2/s)
ρ_0	Density of the fluid (kg/m^3)
μ_0	Molecular viscosity ($kg/m\ s$)
ν_t	Turbulent viscosity (m^2/s)
\bar{p}	Pressure
k	Turbulent kinetic energy
β	Expansion coefficient ($1/K$)
g_i	Gravity acceleration vector in the i -direction (m/s^2)
R	Velocity ratio of the jet to the cross-flow
Pr	Prandtl number
Pr _t	Turbulent Prandtl number
V_0	Streamwise velocity in the side-channel inlet (m/s)
A_0	Cross-sectional area in the side-channel inlet (m^2)
d	Side- and main-channel depth (m)
Fr _{observed_i}	Experimental results
Fr _{predicted_i}	Simulation results
U	Streamwise velocity in the cross-flow inlet (m/s)
Q_0	Flow rate in the side-channel inlet (m^3/s)
C_1, A_s, U^*	Related to the turbulence model
y_m	x_j Coordinate of T_m (m)
$\bar{u}_i, \bar{u}_j, \bar{u}_k$	Velocity components in the $i, j,$ and k direction (m/s)
x_i, x_j, x_k	Cartesian coordinates in the $i, j,$ and k direction (m)
λ_2	Lambda-2 criterion
n	Number of data
I	Spatial index
KK	Time-series index (s)

1 Introduction

The water used in power stations for cooling purposes is often released as thermal effluent at an elevated temperature to the nearby aquatic system in the form of turbulent buoyant jets. The side surface jet discharge using open channels is the cheapest form of waste disposal into water bodies due to constructional economy. The insufficient disposal of thermal effluent can result in serious environmental issues for the aquatic environment [1, 2]. Therefore, the proper understanding of the dispersion, transportation, and mixing processes is necessary for the design of a heat disposal system and the assessment of environmental impact.

In general, the flow structure of the side surface discharge is primarily determined by the momentum ratio between the two tributaries, the magnitude and angle ratio between the tributaries and main channel, and concordance of the channel beds at the confluence entry [3]. Also, the density difference between the effluent and ambient water generates negatively/positively buoyant jets, which follow different flow structures and mixing patterns. Over the past decades, considerable experimental efforts have been carried out to predict the behavior of a thermal pollutant discharged from a side channel leading to a lot of primary findings. Motz and Benedict [4] and Stolzenbach and Harleman [5] experimentally investigated surface discharge of hot water in a deep open-channel cross-flow. Carter et al. [6] and Carter and Regier [7] studied a thermal plume discharged through a side channel with the various depths of cross-flow. Abdelwahed [8] conducted experiments on discharging the heat pollutant from a side channel into a wide open channel influenced by a cross-flow. He et al. [9] reported experimental results of local mean velocity, turbulence quantities, and temperature for

a buoyancy wall jet injected in the opposite direction of the cross-flow. Abessi et al. [10] investigated the negatively buoyant effluent from a side channel in a homogeneous resident fluid. They analyzed flow-mixing behavior using digital video recordings and determined the plume trajectories by using the data obtained from the probe. Teng et al. [11] experimentally studied the effects of a lateral discharge on turbulence characteristics in an open channel with vegetation. They compared their results with the flow field without vegetation. There have also been some field studies in connection with the problems of thermal surface discharge from power plants [12,13]. Shah et al. [14] measured the thermal dispersion of the heated effluent from a nuclear power plant in the field. However, experimental and field studies not only cannot produce detailed flow information and elucidate the evolution of vortex structures, but also are time-consuming and expensive.

Several semiempirical mathematical models, such as Roberts, Snyder, and Baumgartner RSB [15–17], CORMIX [18], and Visual Plumes [19] have been developed, using the results of laboratory measurements and field data. These models, often called plume models, effectively predict general discharge features such as centerline, average dilution, and the location of trajectory under steady-state conditions. Palomar et al. [20] carried out a detailed analysis of the main assumptions, abilities, limitations, and reliability of the Visual Plumes and CORMIX models. Palomar et al. [21] comprehensively validated the Visual Plumes and CORMIX models in comparison with the experimental data of saline water jets in stagnant and dynamic environments. Doneker et al. [22] examined the design of a multiport diffuser which discharged a dense flow in a river using CORMIX. It is important to keep in mind that semiempirical mathematical models are developed based on the simplification of complex mixing processes and cannot provide the details of three-dimensional structures and the temperature distribution in the zone of mixing [23]. An alternative is to use numerical models which simulate three-dimensional structures of turbulent flows at a much lower cost and in detail.

Numerical simulation has been evaluated in various turbulent buoyant jets issues such as sewage disposal from the bottom of a large water body in the cross-flow by a single or multiport pipeline diffusers [24–31], and simulating horizontal wall jets [32–35]. In the case of side surface jet discharge, McGuiirk and Rodi [36] performed the first numerical studies on pollutants discharged from a side channel. They carried out a two-dimensional numerical simulation of the thermal flow discharge. McGuiirk and Rodi [37] developed a three-dimensional numerical model to simulate thermal surface discharge in a stagnant water body from the side channel. Wang and Cheng [38] performed a three-dimensional numerical simulation of the side discharge in a cross-flow channel in steady-state conditions using a commercial code (FLUENT 4.4). Their focus was on the effects of bed roughness and jet width ratio on the flow structure of the recirculation zone. Yu and Righetto [39] developed a depth-averaged turbulence model to study a side thermal jet discharged into a rectangular cross-flow channel. Craft et al. [40] applied different near-wall treatments and turbulence closures to compute a two-dimensional buoyant upward-moving wall jet injected into a downward-directed cross-flow. Addad et al. [41] studied a downward hot wall jet discharged against a cold upward cross-flow by large Eddy simulations (LESs). Tang et al. [23] numerically simulated the initial mixing in the near region of side thermal discharge for a real-life configuration. The domain decomposition method with multilevel embedded overset grids was applied to model the complexity of real-life diffusers. Kim and Cho [42] studied the hot water discharged from the surface and submerged side outfalls in shallow and deep cross-flow using the FLOW-3D model. They applied the renormalization group (RNG) k - ϵ model to simulate the turbulent flow field in steady-state conditions. Peng et al. [43] solved the two-dimensional steady-state shallow water equations using the lattice Boltzmann method to simulate the temperature and flow field of an open channel with a side discharge. They investigated the recirculation zone length for a different side to cross-flow channel velocity ratios. Tay et al. [44] investigated both the main patterns of circulation and the effects of temperature and salinity changes on the southern basin of Tauranga Harbour using the ELCOM model. Constantinescu et al. [3] used an eddy-resolving simulation (DES) to explore the three-dimensional structure of the instantaneous and time-averaged flow at an asymmetrical river confluence for which the momentum ratio is close to 1. They showed how large-scale coherent structures, such as mixing interface eddies, SOV cells, and locally generated vortical features, influence patterns of the turbulent kinetic energy and mean streamwise velocity induced by the complex geometry of the confluence. Penna et al. [45] performed simulations using the PANORMUS code to study the effect of the junction angle on turbulent flow at a hydraulic confluence in the same density. The numerical model solves three-dimensional Reynolds-averaged Navier–Stokes (RANS) equations with the k - ϵ turbulence closure model.

Existing studies on a side surface thermal buoyant jet discharged in the same depth cross-flow have mainly focused on the steady-state flow behavior, while the formations and evolutions of unsteady structures have been ignored. However, understanding the mixing process and evaluating coherent structures is essential to designing and controlling a side surface waste disposal system. In this paper, the three-dimensional features

and the mixing characteristics of the hot water discharged from the side channel in the cross-flow using the OpenFOAM numerical model are investigated in detail. The governing equations are based on unsteady Reynolds-averaged Navier–Stokes (URANS) equations closed with the realizable k - ε turbulence model. The instantaneous and time-averaged contour of flow and temperature fields has been studied to identify flow patterns, coherent structures, and instability mechanisms. The structural features are visualized using a vortex core line detection algorithm named Lambda-2 and the line integral convolution technique. The effect of the velocity ratio of the jet on cross-flow and a densimetric Froude number is studied on the dilution of the hot water flow. The temperature and velocity magnitude contours along with some statistical analysis including the probability density function, power spectral density analysis, temporal mixing deficiency, and spatial mixing deficiency are presented to further explore the mixing process.

2 Theoretical and computational frameworks

2.1 Governing equations

The unsteady Reynolds-averaged Navier–Stokes equations with Boussinesq approximation for buoyancy effects in incompressible fluids are expressed as [44]

$$\frac{\partial \bar{u}_j}{\partial x_j} = 0, \quad (1)$$

$$\begin{aligned} \frac{\partial \bar{u}_i}{\partial t} + \frac{\partial}{\partial x_j} (\bar{u}_j \bar{u}_i) - \frac{\partial}{\partial x_j} \left\{ (\nu_0 + \nu_t) \left(\frac{\partial \bar{u}_i}{\partial x_j} + \frac{\partial \bar{u}_j}{\partial x_i} \right) - \frac{2}{3} \left(\frac{\partial \bar{u}_k}{\partial x_k} \right) \delta_{ij} \right\} \\ = - \frac{\partial}{\partial x_i} \left(\frac{\bar{p}}{\rho_0} + \frac{2}{3} k \right) + g_i (1 - \beta (\bar{T} - T_k)), \end{aligned} \quad (2)$$

where g_i is the gravity acceleration vector in i -direction, t is time, \bar{u}_i , \bar{u}_j , and \bar{u}_k are the velocity components in the i , j , and k direction, respectively, x_i , x_j , and x_k are Cartesian coordinates, δ_{ij} and \bar{p} are the Kronecker delta function and pressure, respectively, $\nu_0 = \mu_0/\rho_0$ is the kinematic viscosity, ρ_0 and μ_0 are the constant density of the fluid and constant molecular viscosity, respectively, ν_t and k are the turbulent viscosity and turbulent kinetic energy, respectively, \bar{T} and T_k are the temperature and a reference temperature in Kelvin (K), respectively, and β is the expansion coefficient with the fluid temperature in K^{-1} .

Yan and Mohammadian [29], Gildeh et al. [34], and Huai et al. [35] simulated turbulent buoyant jets by the realizable k - ε model proposed by Shih et al. [46]. The turbulence kinetic energy and dissipation rate equations of this turbulent model are expressed as

$$\frac{\partial k}{\partial t} + \frac{\partial}{\partial x_j} (\bar{u}_j k) = \frac{\partial}{\partial x_j} \left[(\nu_0 + \nu_t) \frac{\partial k}{\partial x_j} \right] + G_k - \varepsilon, \quad (3)$$

$$\frac{\partial \varepsilon}{\partial t} + \frac{\partial}{\partial x_j} (\bar{u}_j \varepsilon) = \frac{\partial}{\partial x_j} \left[\left(\nu_0 + \frac{\nu_t}{1.2} \right) \frac{\partial \varepsilon}{\partial x_j} \right] + C_1 \sqrt{2 S_{ij} S_{ji}} \varepsilon - \frac{1.9 \varepsilon^2}{k + \sqrt{\nu \varepsilon}}, \quad (4)$$

where $S_{ij} = \frac{1}{2} \left(\frac{\partial \bar{u}_j}{\partial x_i} + \frac{\partial \bar{u}_i}{\partial x_j} \right)$ is the mean strain rate, and the turbulence viscosity is calculated as

$$\nu_t = \left(\frac{1}{4.0 + A_s U^* \frac{k}{\varepsilon}} \right) \frac{k^2}{\varepsilon}. \quad (5)$$

Shih et al. [46] presented relationships to calculate C_1 , A_s , and U^* . The temperature distribution of the thermal plume is determined by the heat advection diffusion derived from the internal energy equation [47]:

$$\frac{\partial \bar{T}}{\partial t} + \frac{\partial}{\partial x_j} (\bar{T} \bar{u}_j) - \frac{\partial}{\partial x_k} \left(\left(\frac{\nu_t}{\text{Pr}_t} + \frac{\nu_0}{\text{Pr}} \right) \frac{\partial \bar{T}}{\partial x_k} \right) = 0. \quad (6)$$

The turbulent Prandtl number (Pr_t) and Prandtl number (Pr) are set to 0.85 and 7, respectively.

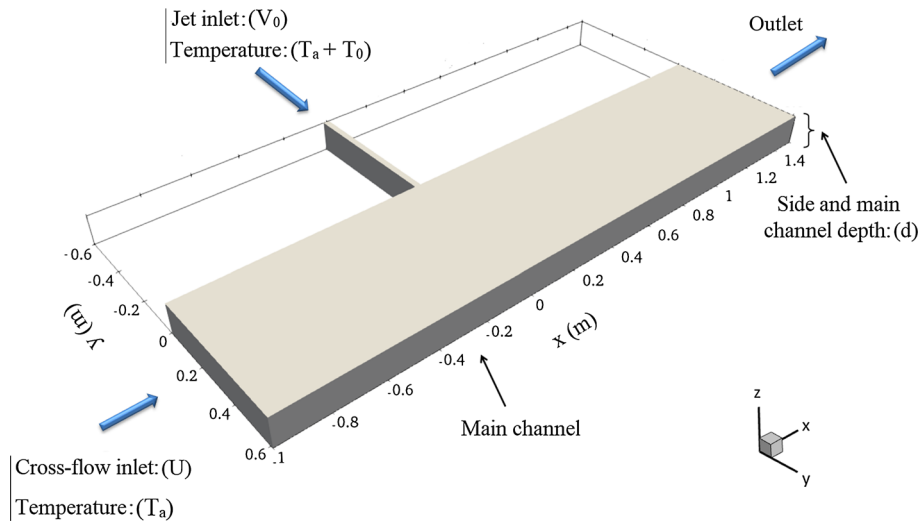


Fig. 1 The computational domain of the hot water discharged from a side channel in a cross-flow

2.2 Numerical method

The open-source CFD software platform OpenFOAM (Open Field Operation and Manipulation), version 5.0.x, is applied for all numerical simulations. The *buoyantBoussinesqPimpleFoam* solver is used as a transient solver for incompressible flows. In the OpenFOAM model, the governing equations are discretized by the finite volume method. Pressures and velocities are coupled implicitly using the Pressure Implicit with Splitting of Operators algorithm [48]. The time derivatives are discretized by the implicit second-order accurate backward scheme. The gradient terms are computed according to the cell limited by the Gauss linear method. The convective terms are discretized using a combined scheme called *filteredLinear2V*. Other gradient terms use either the Gauss linear or the Gauss limited linear scheme. The laplacian term is discretized by Gauss linear limited schemes. The generalized geometric–algebraic multi-grid method with Gauss–Seidel smoother is applied for the pressure field with a tolerance of $10e-6$. The preconditioned bi-conjugate gradient solver with diagonal incomplete LU (DILU) preconditioner is used for the velocity field with a tolerance ($= 10e-8$) for each component, while the stabilized preconditioned (bi-) conjugate gradient method, for both symmetric and asymmetric matrices, with DILU preconditioner is applied for T , k , and ε with a tolerance ($= 10e-8$).

2.3 Computational domain and boundary conditions

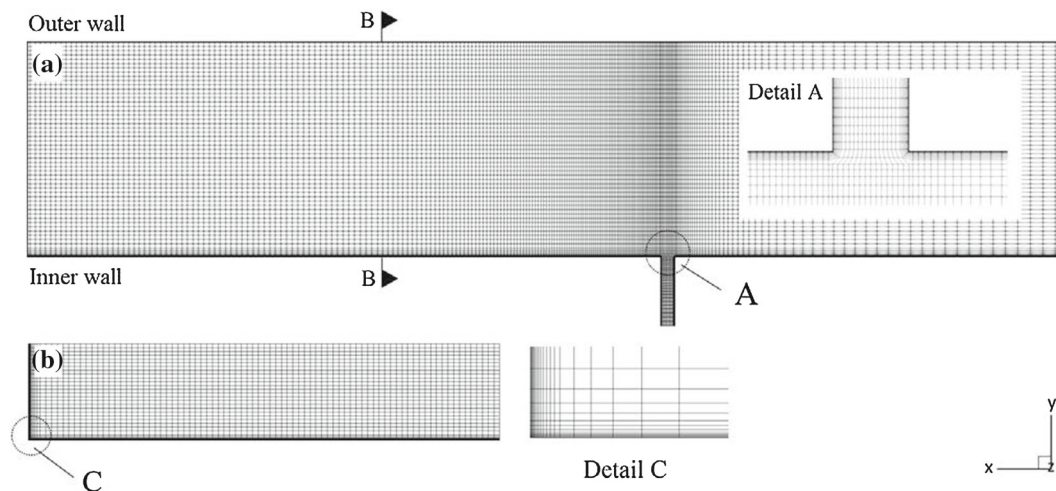
The numerical simulations reproduce several laboratory experiments described in Abdelwahed [8]. All numerical simulations are done in a computational domain with 0.61 m width for the cross-flow channel and 0.025 m width for the side channel. The main-channel length is 1.5 m at the side-channel downstream to simulate the transverse mixing of these currents. The branch-channel length is set to 0.6 m to develop the flow field. Figure 1 shows the computational domain, together with some details. The air effect is neglected.

The experimental conditions and recirculation eddy length (L) of the chosen experiments are summarized in Table 1. U , d , Q_0 , T_a , T_0 , $F_0 (= g (\Delta\rho/\rho) Q_0)$, and $R = V_0/U$ are the streamwise velocity of the cross-flow inlet, side- and main-channel depth, flow rate of the side-channel inlet, temperature of the cross-flow inlet, temperature difference between the side and main channels, buoyancy flux, and streamwise velocity ratio of the side-channel inlet (V_0), and cross-flow inlet (U), respectively (Table 1).

The uniform temperature and velocity are defined in cross-flow and jet inlets. The no-slip boundary condition is applied to all walls for the velocity variable. Besides, adiabatic conditions are enforced for the temperature at solid boundaries. Moreover, the standard wall function provided by OpenFOAM was used for ν_t (*nutUSpaldingWallFunction*), ε (*epsilonWallFunction*), and k (*kLowReWallFunction*) in the walls, which are suitable for a wide range of z^+ values. The symmetry condition is used in the free surface. A zero gradient is used for the pressure on all boundaries except the cross-flow outlet, where the pressure is fixed to zero.

Table 1 The experimental conditions and recirculation eddy length (L) of experiments performed by Abdelwahed [8]

Test no.	U (cm/s)	d (cm)	Q_0 (cm ³ /s)	T_a (°C)	T_0 (°C)	$R = V_0/U$ (-)	F_0 (cm ⁴ /s ³)	L (m)
1E	6.12	6.00	157.73	21.2	7.80	1.69	309.43	0.5785
2E	6.06	9.00	457.73	20.20	7.80	1.14	298.01	0.3563
3E	8.10	9.08	234.89	20.10	5.00	1.26	267.94	0.4213
4E	6.01	12.5	181.851	19.40	6.50	0.95	269.92	0.2606
5E	5.99	12.5	272.78	18.90	4.40	1.44	256.08	0.5216
6E	6.18	12.5	363.70	18.70	3.35	1.86	250.57	0.765
7E	6.06	12.5	151.54	18.40	7.70	0.79	261.68	0.1838
8E	6.05	12.5	454.63	18.20	2.75	2.37	246.83	1.045

**Fig. 2** The generated grid **a** plan view and **b** B–B cross-sectional view

2.4 The grid and time-step independence study

Figure 2 shows the plan and cross-sectional views of the structured mesh utilized in the computational domain of the numerical simulations. The x -mesh size is smaller near the side channel and then increases toward the main-channel downstream. The x -mesh size finally reaches a constant value (Δx). Due to the velocity gradient, the first grid is adjusted near the inner wall and bed as $y^+ (= y_2 u_* / \nu)$ and $z^+ (= z_2 u_* / \nu)$ are always less than 1. u_* is the friction velocity and y_2 and z_2 are the first cell distance to the inner wall and bed, respectively. The maximum y^+ approximately is less than 20 on the outer wall. The y - and z -mesh size is increased by the rate of 1.2. The y - and z -mesh sizes finally reach constant values (Δy , Δz).

The sensitivity analysis of the numerical simulation results in the grid is carried out for the 1E test by three different meshes. $\Delta x \times \Delta y \times \Delta z$ values are $0.01125 \times 0.009375 \times 0.00625$, $0.009 \times 0.0075 \times 0.005$, and $0.0072 \times 0.006 \times 0.004$ m for the coarse, medium, and fine grids, respectively. The grid size of medium and fine grids has been refined with a coefficient of 0.8 in the x , y , and z -direction in comparison with the coarse, medium, and fine grids, respectively. The number of grid points is, respectively, 1122940, 777331, and 557109 in the fine, medium, and coarse grids for the 1E test. The time step (Δt) is set 0.05 s in the coarse grid. Δt is also simultaneously reduced by a coefficient of 0.8 in the medium and fine grids to evaluate the independence of the results to the time step. It is set to 0.04 and 0.032 s in the medium and fine grids.

The time-averaged velocity magnitude, kinetic energy, and epsilon profiles of the 1E test are recorded at 0.5 cm under the free surface and $x = 0.10$ m of the main channel. The numerical simulation results are approximately similar for three analyses, although the medium and fine grids which predicted the same time-averaged velocity magnitude profile near the inner wall and patterns of time-averaged kinetic energy and epsilon profiles are similar for the medium and fine grids (Fig. 3). Therefore, the time step of 0.04 s with the medium grid to save on the cost of calculations is chosen to investigate the flow structure and mixing patterns.

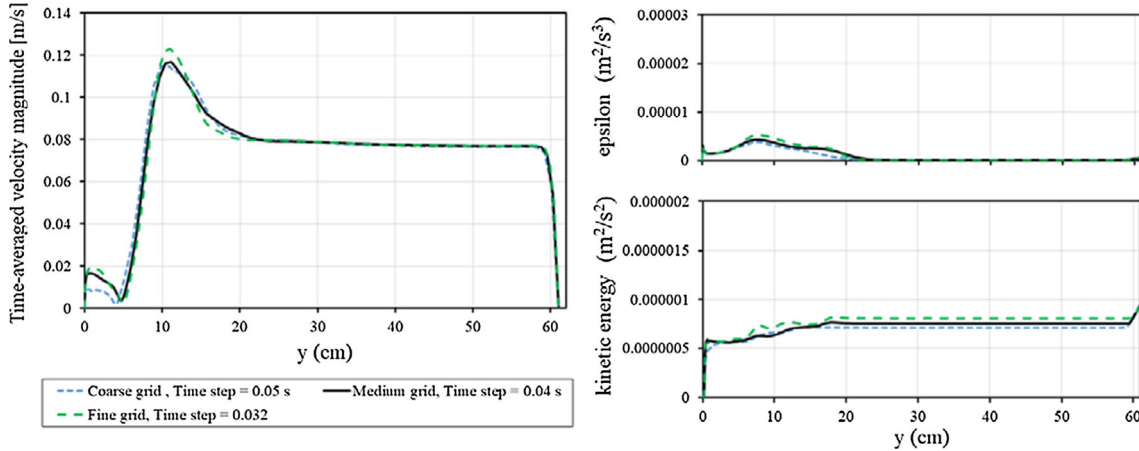


Fig. 3 The sensitivity analysis of time-averaged velocity magnitude, kinetic energy, and epsilon profiles to the grid and time step

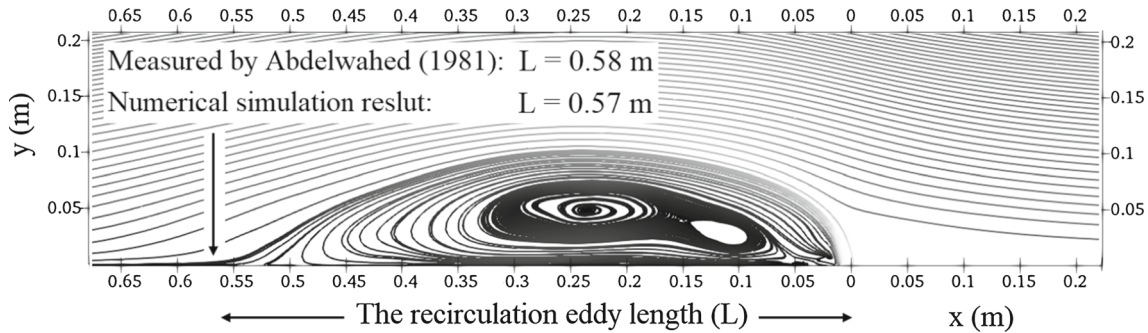


Fig. 4 Streamlines illustrated by the time-averaged flow field of 1E test in the plan view

2.5 Model verification

In this paper, experiments performed by Abdelwahed [8] are selected to verify the numerical model. The determination coefficient (R^2) and mean absolute relative error (MARE) indices are used to assess the accuracy of the numerical simulation results as follows:

$$R^2 = \left(\frac{\sum_{i=1}^n \left(Fr_{\text{observed}_i} - \sum_{i=1}^n Fr_{\text{observed}_i} / n \right) \left(Fr_{\text{predicted}_i} - \sum_{i=1}^n Fr_{\text{predicted}_i} / n \right)}{\sqrt{\sum_{i=1}^n \left(Fr_{\text{observed}_i} - \sum_{i=1}^n Fr_{\text{observed}_i} / n \right)^2} \sqrt{\sum_{i=1}^n \left(Fr_{\text{predicted}_i} - \sum_{i=1}^n Fr_{\text{predicted}_i} / n \right)^2}} \right)^2, \quad (7)$$

$$\text{MARE} = \frac{1}{n} \sum_{i=1}^n \frac{|Fr_{\text{observed}_i} - Fr_{\text{predicted}_i}|}{Fr_{\text{observed}_i}}, \quad (8)$$

where n is the data number and Fr_{observed_i} and $Fr_{\text{predicted}_i}$ are the experimental and simulation results, respectively.

The heated full-depth discharge is strongly affected by a recirculation region immediately formed after the jet next to the main-channel wall, which consists of the side channel (inner wall). Abdelwahed [8] reported the recirculation eddy length of 0.5785 m in the 1E test. As shown in Fig. 4, there is a good consistency between the simulated ($L = 0.57$ m) and reported results.

When the recirculation zone ends, the heat flow lifts off from the channel bottom due to the buoyancy and creates a plume surface. The temperature half-thickness, in which the temperature is equal to the half of the temperature at the water surface, is used to present the thermal cross section. Figure 5a, b shows the cross section of plume flow at $x = 15$ and 30 cm located near the discharged jet within the recirculating zone and

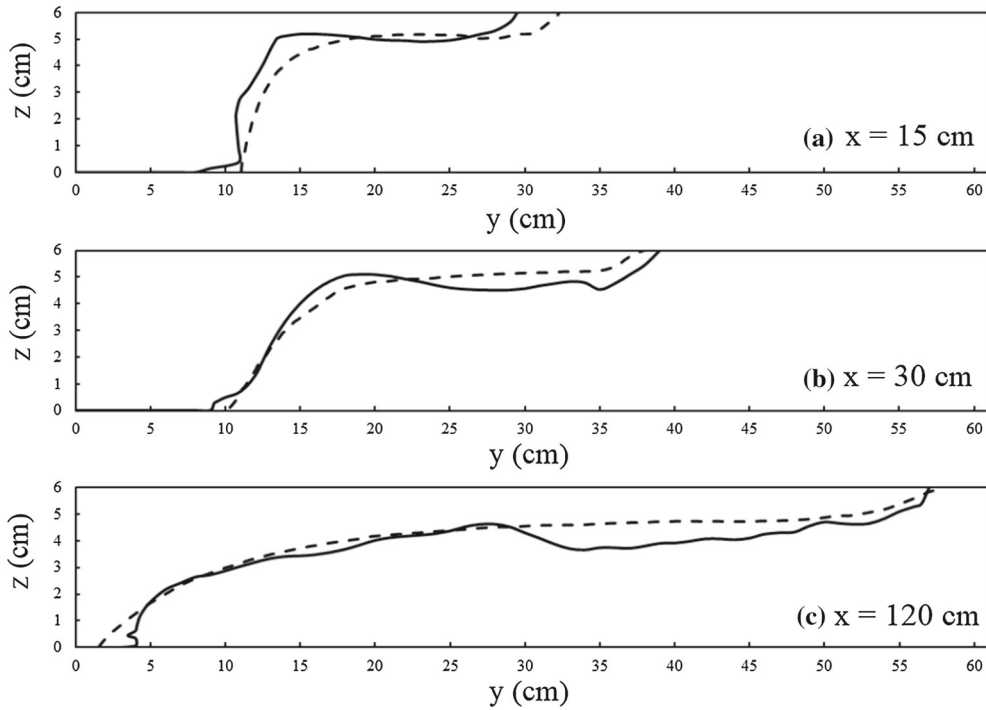


Fig. 5 Thermal cross sections of the full-depth plume flow in 1E test; numerical results (solid line), experimental results (dashed line)

slightly lower than the recirculating zone, respectively. The numerical model simulates the separation of the plume flow from the channel bottom well. At $x = 15$ cm, the length of the spreading plume flow is predicted smaller than the experimental result at the free surface (Fig. 5a). At $x = 30$ cm, the plume flow is affected by both the jet momentum and buoyancy. In Fig. 5b, the length of the spreading plume is slightly predicted greater than the experimental result at the free surface. The far field of plume flow is strongly affected by the buoyancy at $x = 120$ cm (Fig. 5c). The numerical model predicted the plume flow length next to the bottom slightly larger than the experimental result. The length of the spreading plume flow is simulated at the free surface with a very good accuracy at $x = 120$ cm.

The time-averaged excess temperature (T) is determined at each node of computational domain as follows:

$$T = \frac{1}{n} \sum_{KK=1}^n (\bar{T} - T_a)_{KK}, \quad (9)$$

where n is the number of the temperature (\bar{T}) recorded at each node and KK is the time-series index. The time duration is set to 110 s in all numerical simulations. The numerical results are recorded at 55 s. Since the number of temperature samples per second is 25 at each node, n is 1375 for all numerical simulations which is similar to the experiments of Abdelwahed [8]. Figure 6 presents the measured and simulated results of T for the 3E test in three depths ($z = 8.58, 6.08, 2.58$ cm) of cross sections located at $x = 12.5, 25, 98$ cm. These selected positions are in the near field to the far field. The near-field flow is mostly influenced by the momentum force of the discharged jet and recirculation zone. The heat flow is mostly affected by the buoyancy force after the recirculation zone (far field). The experimental and numerical results of T show a good agreement (Fig. 6). However, applying the symmetry boundary condition, a small difference can be seen between the numerical and experimental results in the near and far field next to the free surface.

T_m , y_m , and $2\eta_m$ are used to describe the jet trajectory at the free surface. T_m is the maximum time-averaged excess temperature at different cross sections. y_m is the x_j coordinate of T_m . $2\eta_m$ is the half-width of T_m along the y coordinate. Abdelwahed [8] defined the length, time, and temperature scales as follows:

$$l_s = \left(\frac{M_0^2}{U F_0} \right)^{1/3}, \quad (10)$$

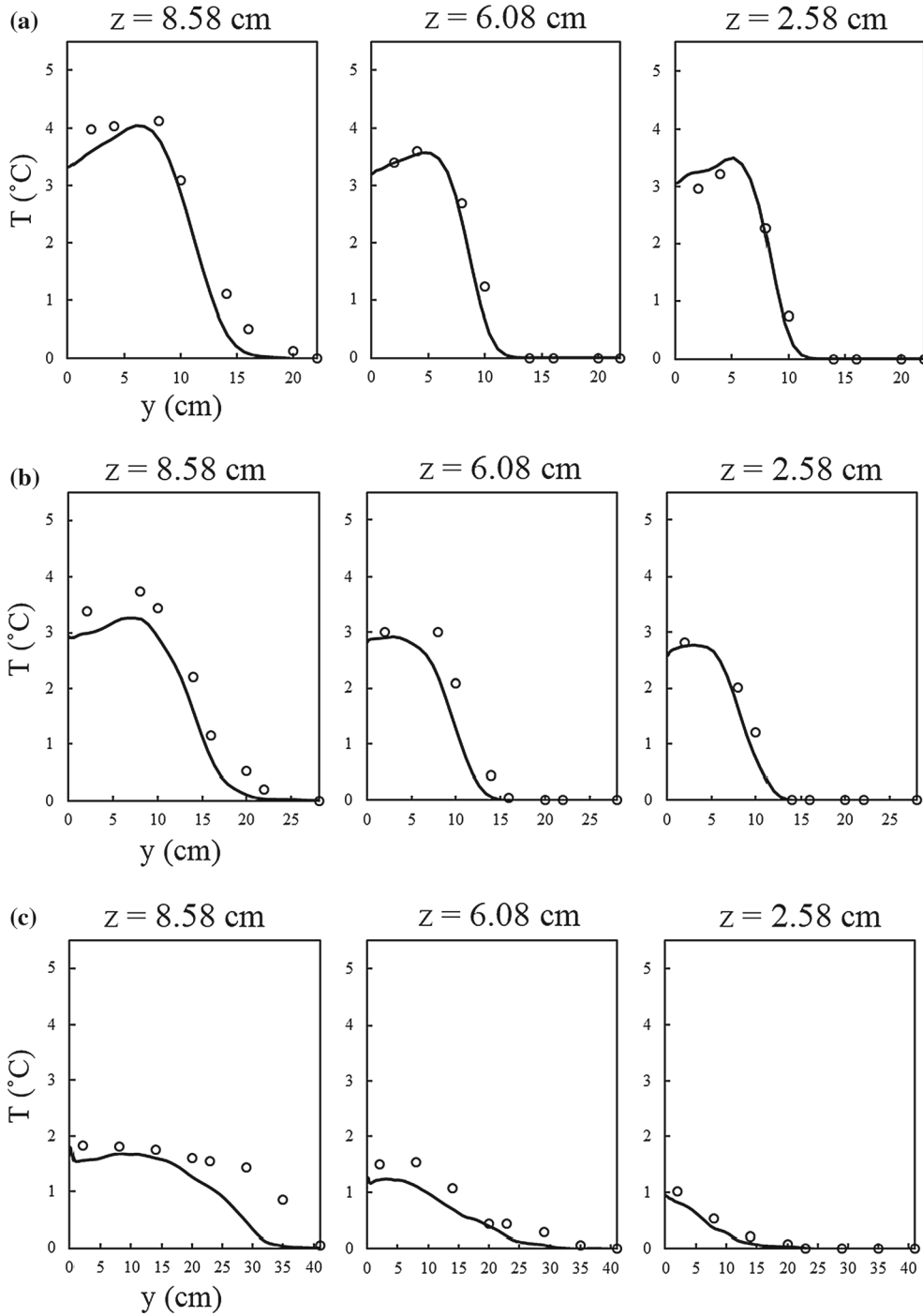


Fig. 6 Experimental (○) and numerical results (solid line) of time-averaged excess temperature for 3E test: **a** $x = 12.5$ cm; **b** $x = 25$ cm; **c** $x = 98$ cm

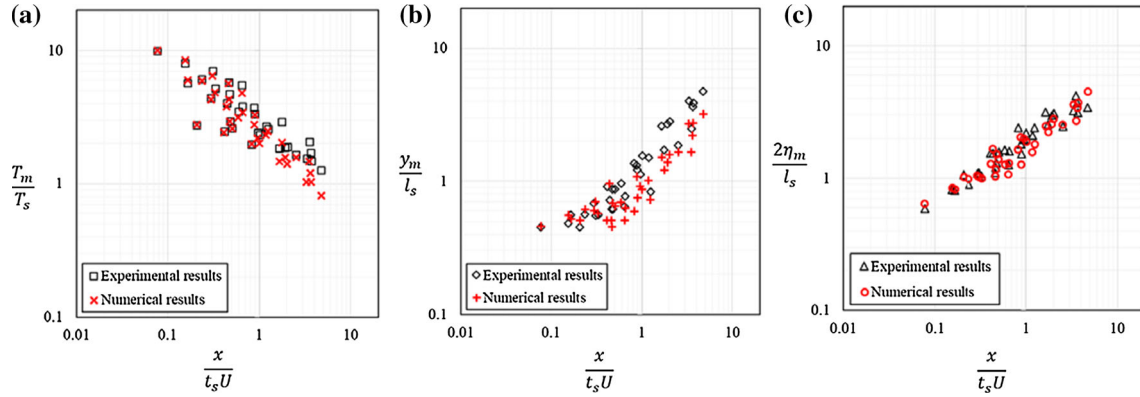


Fig. 7 **a** The maximum time-averaged excess temperature, **b** the location of the maximum time-averaged excess temperature, and **c** the half-width of the maximum time-averaged temperature at different longitudinal locations along the cross-flow of 1–8E tests

$$t_s = \frac{M_0}{F_0}, \quad (11)$$

$$T_s = \frac{\Gamma_0}{U l_s^2}, \quad (12)$$

where $M_0 = V_0^2 A_0 + \frac{1}{2\rho} g (\Delta\rho) dA_0$ is the flow force and $\Gamma_0 = T_0 Q_0$ is the heat flux of the discharged jet. A_0 is the cross-sectional area of the side channel. The predicted results of T_m , y_m , and $2\eta_m$ are compared with the experimental results of the 1-8E tests in Fig. 7. MARE values of the results, presented in Figs. 7a–c, are 11.92%, 26.33%, and 13.60%, respectively. R^2 values are 98.28%, 93.47%, and 80.23% for these results. A good agreement can be seen between the numerical and experimental results. However, the numerical model predicts T_m and y_m slightly smaller than the experimental results after the recirculation zone (Figs. 7a, b).

Buoyancy effects are not considered in Eqs. (3) and (4) of the turbulence model. Thus, the terms $G_{bk} = -\beta g_i u_i' \overline{T'}$ and $G_{b\varepsilon} = C_{1\varepsilon} \frac{\varepsilon}{k} C_{3\varepsilon} G_{bk}$ are, respectively, added to the k and ε equations to investigate buoyancy effects. $\overline{u_i' T'}$ ($= -\frac{\nu_t}{Pr_t} \frac{\partial \overline{T}}{\partial x_i}$) is the turbulent heat flux. β is considered as:

$$\beta = -\frac{1}{\rho} \left(\frac{\partial \rho}{\partial \overline{T}} \right). \quad (13)$$

The density is calculated using the UNESCO equation of the state [49] as follows:

$$\rho = 999.842594 + 6.793952 \times 10^{-2} \overline{T} - 9.095290 \times 10^{-3} \overline{T}^2 + 1.001685 \times 10^{-4} \overline{T}^3 - 1.120083 \times 10^{-6} \overline{T}^4 + 6.536332 \times 10^{-9} \overline{T}^5. \quad (14)$$

Henkes et al. [50] propose $c_{\varepsilon 3} = \tanh \left| \frac{\sqrt{\overline{u_i + \overline{u_j}}}}{\overline{u_k}} \right|$ in the buoyancy term of the ε equation. Figure 8 indicates the T_m profiles for the turbulence equations with and without buoyancy effects in comparison with the experimental results. The modified turbulence equations do not improve the numerical simulation results (Fig. 8).

3 Flow structure

The surface discharge of the jet from the side channel causes complex vortical structures, which are the interactions between jet, cross-flow, and wall boundary layers. These structures consist of large scales in near fields around the discharge location to small scales in far fields of the discharge location. In this section, the λ_2 criterion is used to visualize 3D coherent structures. This criterion is defined as negative value of the second eigenvalue of the symmetry square of the velocity gradient tensor. See Jeong and Hussain [51] for more information regarding the λ_2 criterion.

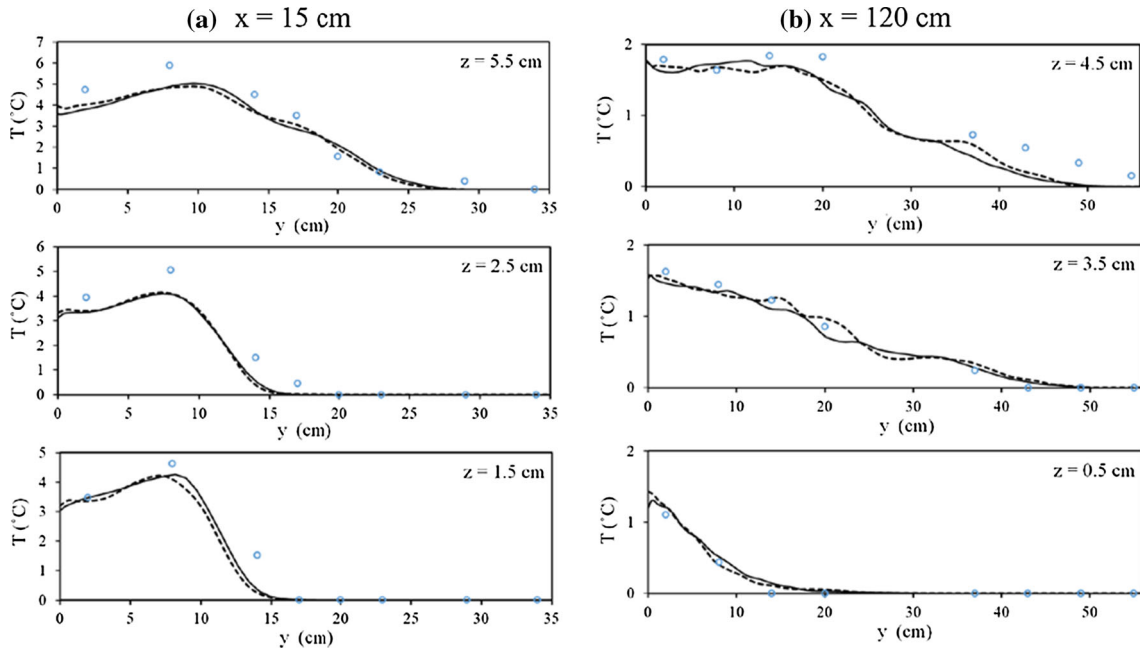


Fig. 8 The time-averaged excess temperature profiles simulated by the turbulence equations with (solid line) and without (dotted line) buoyancy effects in comparison with the experimental results (o)

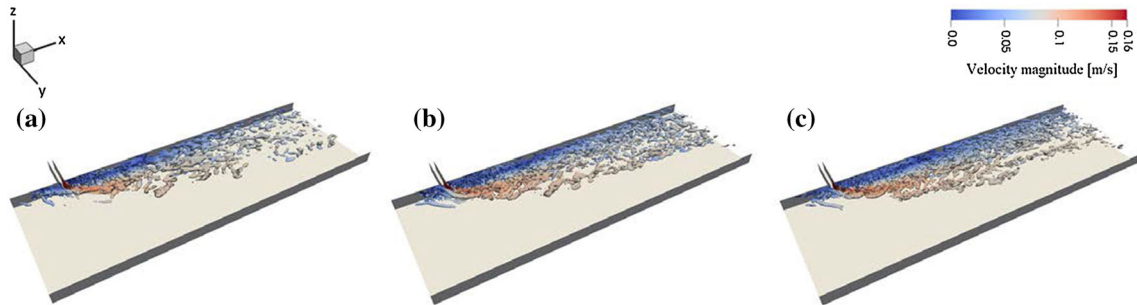


Fig. 9 The iso-surface of the $\lambda_2 (= 0.2)$ criterion colored by the instantaneous velocity magnitude for **a** coarse, **b** medium, and **c** fine grid

The instantaneous vorticity is presented for the 1E test simulated with the coarse, medium, and fine grids (described in Sect. 2.4) in Fig. 9. All vortices are recorded after 110 s with $\lambda_2 = 0.2$. All grids can simulate the large scale of the coherent structures in the near field. The coherent structures with the small scales are in the far field due to the high mixing of the discharged flow. The fine and medium grids predict the small scale of the coherent structures in the far field with more detail than the coarse grid. Hence, the medium grid is chosen for the numerical simulations.

The 8E test is selected to investigate the vortex structures. Figure 10 shows the instantaneous vorticity magnitude colored with the temperature. Large-scale coherent structures dominate near the discharge location, while the final structures are often smaller and more chaotic than the primary structures. Jet shear-layer vortices are perpendicular to the cross-flow close to the discharge location. These vortices slightly continue toward the cross-flow downstream and then collapse into smaller structures due to instabilities and entrainment with the cross-flow. The shear-layer vortices illustrated in the 8E test have also been observed in other tests, which are ignored here for brevity.

The buoyant surface jet acts as an obstacle in the cross-flow near the discharge location. The pressure is enhanced at higher levels due to the flow velocity increasing from the bed to the water surface. Thus, a pressure gradient is created in the jet direction from the top layer to the bottom layer. This gradient causes a flow from the top layer to the bottom layer. This flow moves upward after the collision with the bed and creates unsteady horseshoe vortices with the cross-flow. Due to the periodicity and weakness of these vortices,

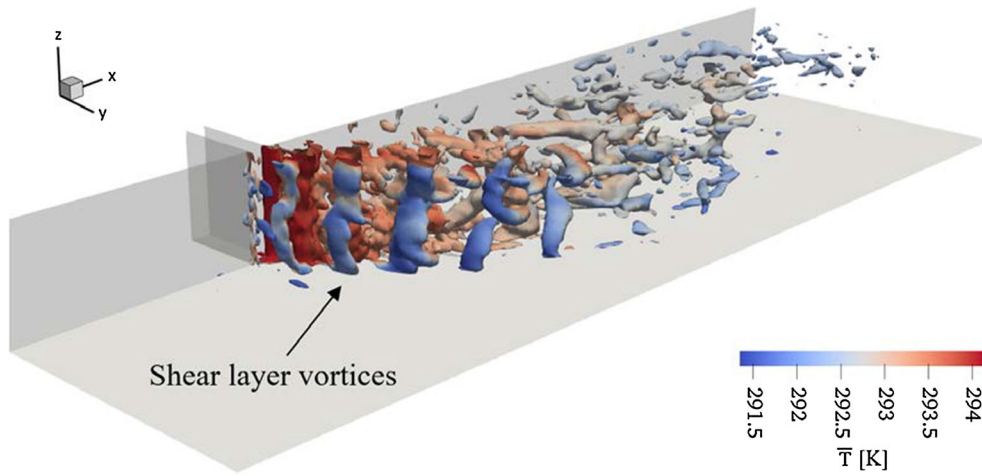


Fig. 10 The iso-surface of the $\lambda_2(= 2)$ criterion colored with the instantaneous temperature of 8E test

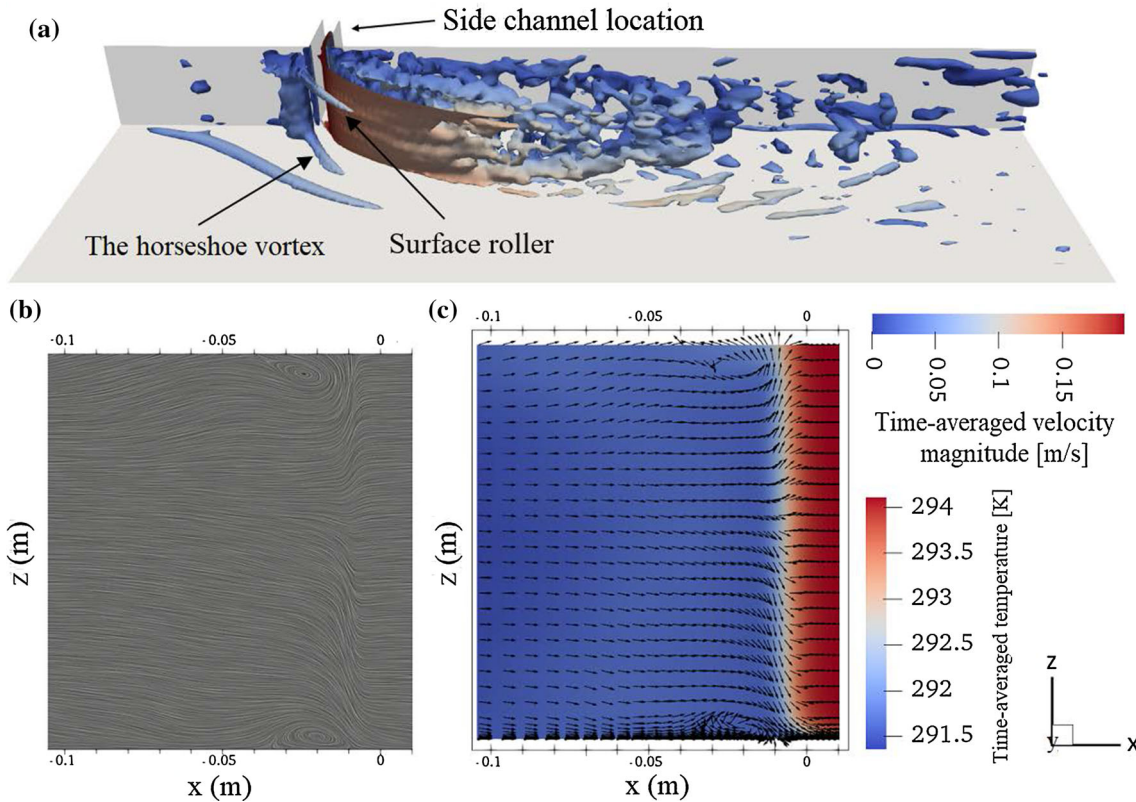


Fig. 11 **a** The iso-surface of $\lambda_2(= 0.1)$ criterion colored by the time-averaged velocity magnitude, **b** two-dimensional streamlines at $y = 0.05$ m, and **c** time-averaged velocity vectors colored by the time-averaged temperature at $y = 0.03$ m

their visualization is not well done by the instantaneous flow fields. A horseshoe vortex is near the shear layer and clings to the bed (Fig. 11a). Figures 11b, c illustrate two-dimensional streamlines visualized by the LIC method and time-averaged velocity vectors colored by the time-averaged temperature in the main-channel cross section located at $y = 0.03$ m. A surface roller is observed at the discharge location upstream near the free surface. This weak vortex slightly surrounds the mixing flow similar to the horseshoe vortex.

Figure 12 shows two-dimensional streamlines in cross sections located at $y = 0.03$ m by the LIC method. For all values of R , the surface roller is formed near the free surface. Only the surface roller occurs, and the horseshoe vortex does not appear for $R = 1.14$. With increasing R values, the horseshoe vortex forms at the

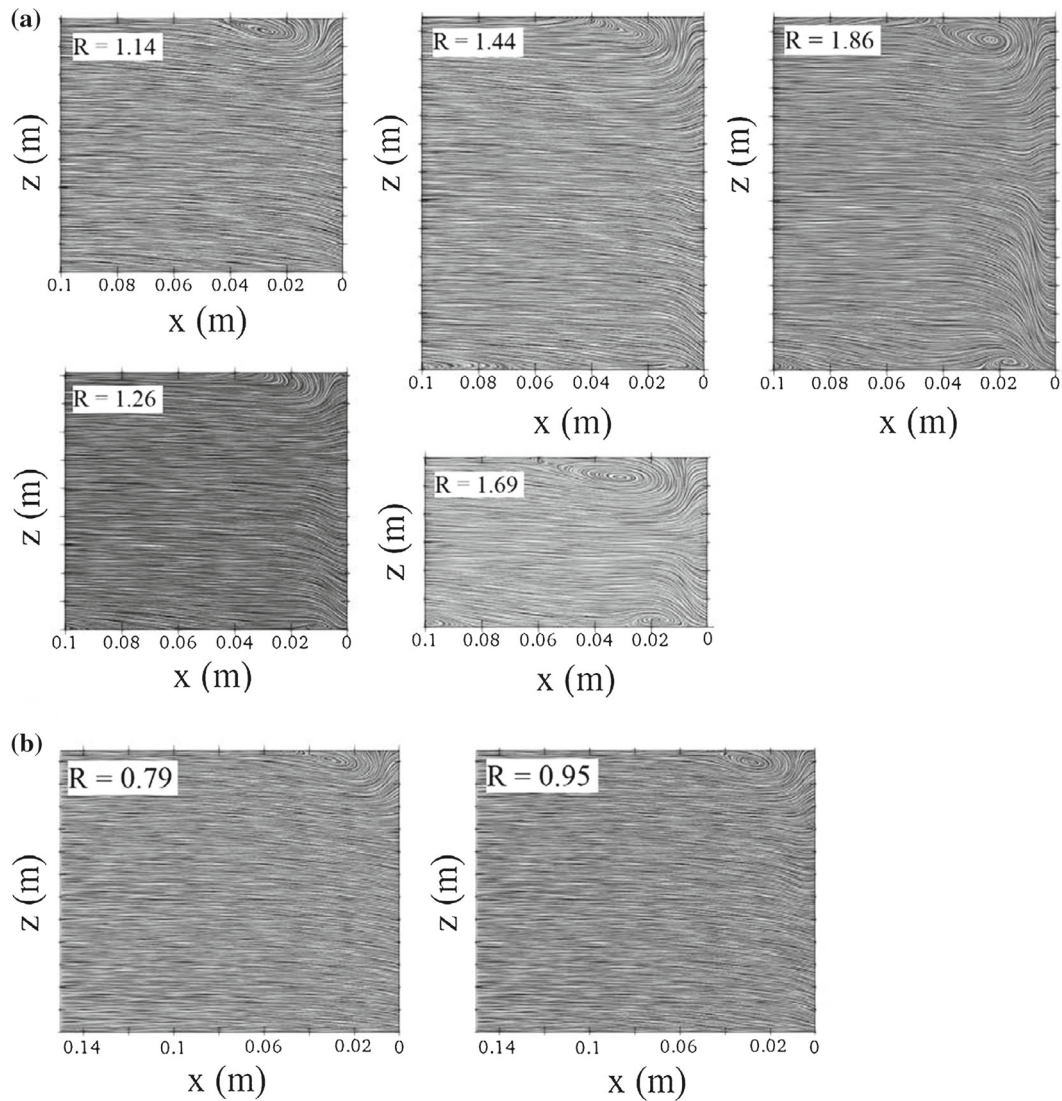


Fig. 12 Two-dimensional streamlines visualized by the LIC method for **a** $R > 1$ and **b** $R < 1$ at $y = 0.03$ m

channel bottom near the discharge site. As R increases, the horseshoe vortex appears upstream of the lateral channel. For $R < 1$, no horseshoe vortex develops and only the surface roller is created (Fig. 12b).

Figure 13 shows instantaneous coherent structures colored with the time-averaged velocity magnitude along the main channel by the iso-surface of the $\lambda_2 (= 2)$ criterion. Four distinct regions can be identified in this figure. The first region is the location of the discussed shear vortices. In the second region ($x = 0.05$ to 0.25), the shear-layer vortices are affected by the recirculation zone and buoyancy. The vortices are drawn inside the recirculation zone and diffused at the free surface by them. These spiral vortices are convected to downstream by the cross-flow. A part of these vortices enters the recirculation zone, and the other part moves downward (third region). After the recirculation zone, the buoyancy force detaches the flow from the bottom and concentrates it at the surface (fourth region). The vortices decrease stronger near the bed than near the free surface in the far fields (Fig. 13). The distinct regions indicated in the 8E test have also been observed in other tests, which are ignored here for brevity.

The perpendicular vortices are converted to parallel vortices with the cross-flow (Figs. 13 and 14). Besides, the vortices near the surface are just drawn in Fig. 14 to simplify the detection of secondary vortices created near the free surface. These secondary vortices are also reported by Weber et al. [52] and have also been observed in other tests, which are ignored here for brevity.

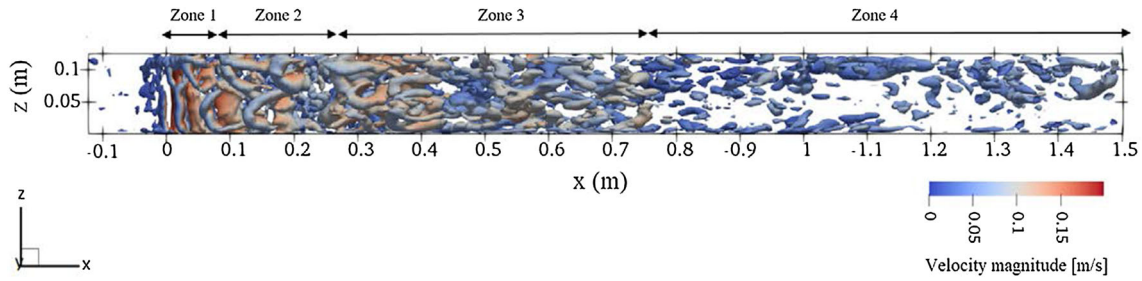


Fig. 13 Instantaneous coherent structures of the $\lambda_2 (= 2)$ criterion in cross-flow direction colored by the velocity magnitude along the main channel

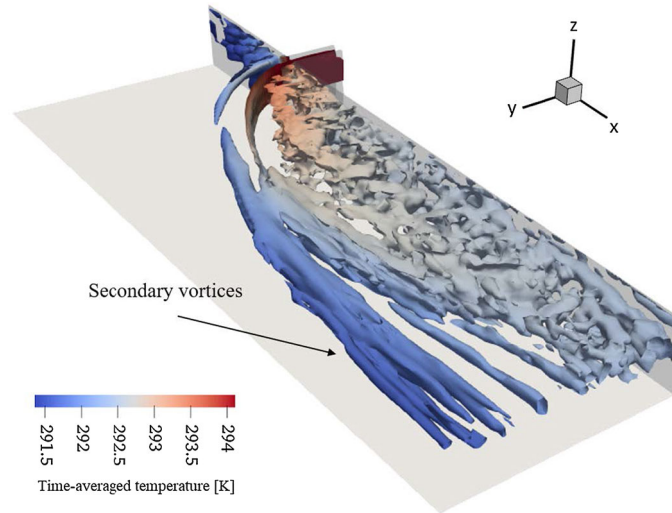


Fig. 14 The iso-surface of the λ_2 criterion colored by the time-averaged temperature

Figure 15 shows two-dimensional streamlines drawn by time-averaged velocity vectors at cross sections located at $x = 12.5, 25, 50, 70,$ and 105 cm. Three-dimensional streamlines derived from the side channel are also provided in this figure. The line integral convolution (LIC) method is used to draw the streamlines. LIC is an effective technique for visualizing vector fields. For more information on this method, refer to Cabral and Leedom [53]. The vortices, which are illustrated based on the time-averaged velocity vectors, are the dominant movement patterns at cross sections of the main channel. Near the discharge location, the flow is affected by the recirculation zone and rotating vortices can be seen close to the inner wall. The effective width of the main channel decreases as the recirculation zone width increases up to $x = 0.5$ m, reaching its minimum there (Fig. 15). The deviation and collision of the cross-flow to the outer wall occur due to the gradual decrease in the effective width of the cross-flow. The secondary currents are formed at $x = 0.5$ m. Weber et al. [54] reported that the cross-flow collision to the outer wall causes the secondary currents at the junction of rectangular channels. The vortices are concentrated near the free surface after the recirculation zone. A similar trend was observed for other R values in the formation and degradation of secondary vortices, which are ignored here for brevity.

In order to investigate the R effect on the secondary flow strength (S_{xy}), the quantitative changes of S_{xy} are explored at cross sections of the cross-flow channel. Shukry [55], while conducting studies on the streamflow at the riverbank, outlines the secondary flow mechanism and introduces the following criterion for S_{xy} :

$$S_{xy} = \frac{\int (\bar{u}_i^2 + \bar{u}_j^2) dA}{\int (\bar{u}_i^2 + \bar{u}_j^2 + \bar{u}_k^2) dA}. \quad (15)$$

This criterion at a given cross section is the kinetic energy ratio of the lateral current and mainstream. Figure 16a, b shows S_{xy} changes along the main channel at different cross sections. The S_{xy} maximum increases with

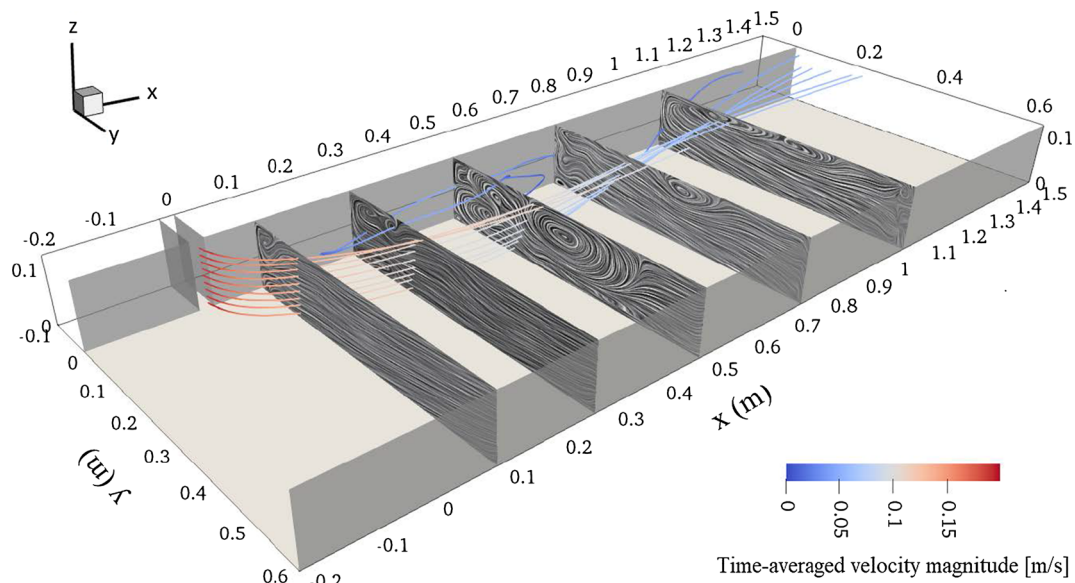


Fig. 15 Three-dimensional and two-dimensional streamlines based on the time-averaged velocity vectors and colored by the time-averaged velocity magnitude

increasing R values. The highest and lowest values of the S_{xy} maximum are at $R = 2.37$ and 0.79 , respectively. The S_{xy} maximum always occurs near the lateral channel and decreases away from the side channel until it reaches almost zero. S_{xy} increases a little after the minimum value and then decreases toward the cross-flow channel downstream. By comparing the flow pattern in Fig. 15 and the S_{xy} value in Fig. 16 for $R = 2.37$, it is observed that the secondary flow strength reaches its minimum value in the area where the effective width of the main channel is the lowest. According to Fig. 16, the development patterns of the secondary flow are almost similar for all R values.

Figure 17 shows the temporal evolution of the temperature in-plane views located at $z = 12$ cm (0.5 cm below the free surface) for the 8E test. The counterclockwise-rotating vortices, called backward-rolling vortices, are observed at the confluence of the jet and cross-flow (windward) because of Kelvin–Helmholtz instability. Zhang and Yang [31] reported the same vortices for the jet flow from the channel bottom with a circular cross section. The gaps between the vortices mix the cross-flow with the jet fluid. This pattern has also been observed for 1-7 E tests that are ignored here for brevity. The diameter of the vortices becomes larger toward the main-channel downstream, and they disappear approximately at $x = 0.5$ m. In other words, the vortices stick to the jet boundary. They slightly move along the jet boundary and then shed in the main channel toward the downstream (vortex shedding). The position of the vortex shedding for other test is discussed in more detail in the following sections. The vortices reserve some fluid with the higher temperatures and transport them to the main-channel downstream before the vortex shedding. This phenomenon can be observed at $x = 0.4$ m to 0.6 m for times 50 to 51 in Fig. 17.

Figure 18 shows the instantaneous streamlines for the 1E test. The recirculation zone is confined to the high-velocity features and inner wall. The velocity in the recirculation zone is lower than the surrounding flow velocity. The turbulent motions can be observed in the recirculation zone structure. A stagnated zone with a lower velocity than its surrounding environment is formed in the confluence upstream. Webber et al. [54] and Best [56] reported a stagnated zone in this region for channel confluences. A retardation area is observed near the side channel (Fig. 18). The retardation zone inside each channel is the result of the flow deflection from the upstream corner of the junction. Velocities are reduced in this region whose size depends on the junction angle [45]. Figure 19 illustrates streamlines near the retardation area for the 1-8E test. Due to the unsteady behavior of the flow, time-averaged velocity vectors have been used to draw streamlines. As can be seen, the elongation of this area decreases to the upstream and width of the main channel with decreasing R value. The retardation area is not detectable for $R < 1$ (Fig. 19b).

The maximum time-averaged velocity magnitude tends to the outer wall toward the main-channel downstream in all tests with $R > 1$. The maximum time-averaged velocity magnitude gradient is closest to the

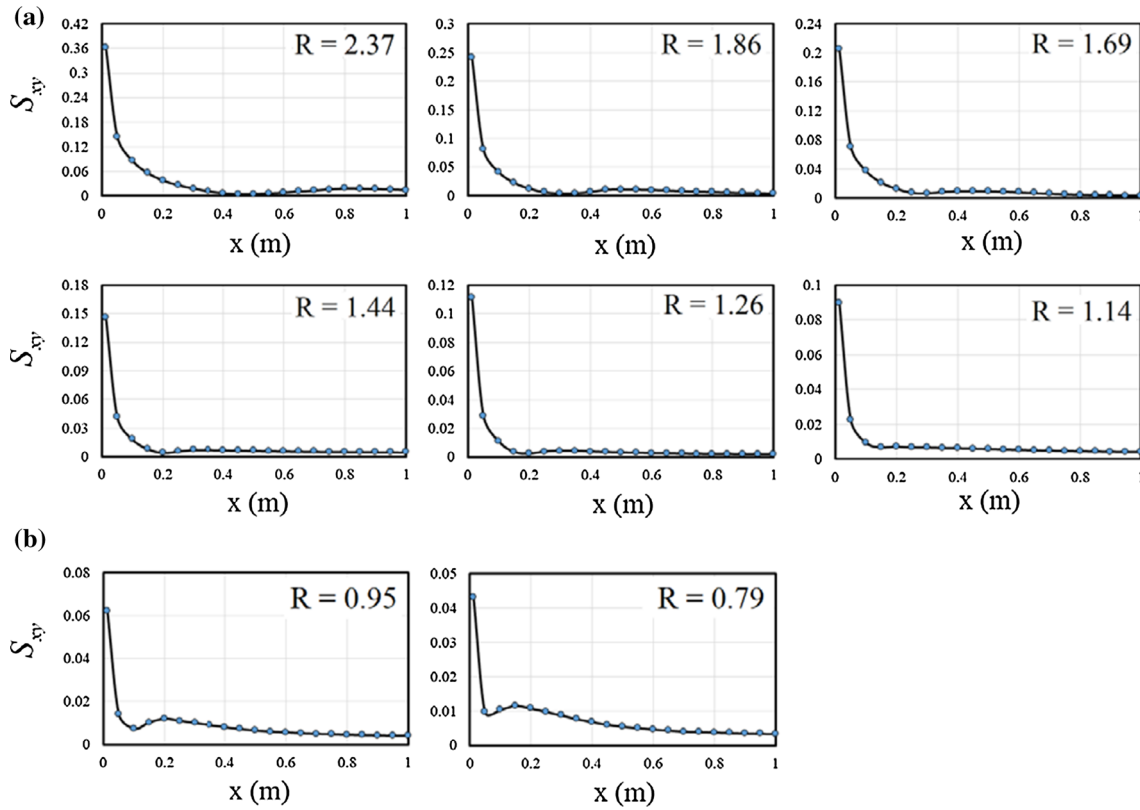


Fig. 16 Secondary flow strength (S_{xy}) variations along cross sections of the cross-flow channel for **a** $R > 1$, and **b** $R < 1$

discharge location and decreases toward the main-channel downstream (Fig. 20). The maximum time-averaged velocity magnitude gets closer to the outer wall toward the main-channel downstream by increasing R (Fig. 20).

Circular cores of columnar vortices are observed in the shear layer (Fig. 21). The maximum velocity magnitude of shear-layer vortices occurs in their center and decreases toward the main-channel downstream. Some vortices gradually fade from the free surface toward the channel bottom which appear again next to the bed, due to spiral vortices of the shear layer (Figs. 13 and 21). This pattern has also been observed in other tests that are ignored here for brevity. Circular cores approximately disappear at $x = 0.5$ m. This distance corresponds to the vortex shading region.

Figure 22 shows the maximum time-averaged excess temperature and velocity magnitude normalized in cross section of tests with $R > 1$:

$$(T_m)_{\text{normalized}} = \frac{T_m - (T_m)_{\text{min}}}{(T_m)_{\text{max}} - (T_m)_{\text{min}}}, \quad (16)$$

$$(U_m)_{\text{normalized}} = \frac{U_m - (U_m)_{\text{min}}}{(U_m)_{\text{max}} - (U_m)_{\text{min}}}. \quad (17)$$

$(U_m)_{\text{normalized}}$ decays faster than $(T_m)_{\text{normalized}}$ for tests with $R > 1$. $(T_m)_{\text{normalized}}$ almost is maximum and constant about $\text{Log}(x) = 0.0$ to 0.01 (jet potential core). $(U_m)_{\text{normalized}}$ immediately decreases with different slopes from the discharge location in the jet potential core. Comparing different tests, it is observed that, in addition to R , the $(U_m)_{\text{normalized}}$ slop also depends on T_0 and d . After the jet potential core, an irregularity is observed in profiles, especially in $(U_m)_{\text{normalized}}$, $(T_m)_{\text{normalized}}$ and $(U_m)_{\text{normalized}}$ increase faster than those in jet potential core. This region is the position where the surface jet sheds in the cross-flow. The irregularity is hardly visible in profiles of $R = 1.14$ because R is close to 1.0 in this test. In the far field from the side channel, the decreasing slope (κ) of $(T_m)_{\text{normalized}}$ and $(U_m)_{\text{normalized}}$ profiles is almost constant and equal. Zhang and Yang [31] reported the same trend to discharge a circular dense jet from the channel bottom with velocity ratios of 2 and 4. Figure 23 shows $(T_m)_{\text{normalized}}$ and $(U_m)_{\text{normalized}}$ at the cross-flow direction and the free surface for 4E and 7E tests (with $R < 1$). Near the discharge location, the $(T_m)_{\text{normalized}}$ and $(U_m)_{\text{normalized}}$ trend is

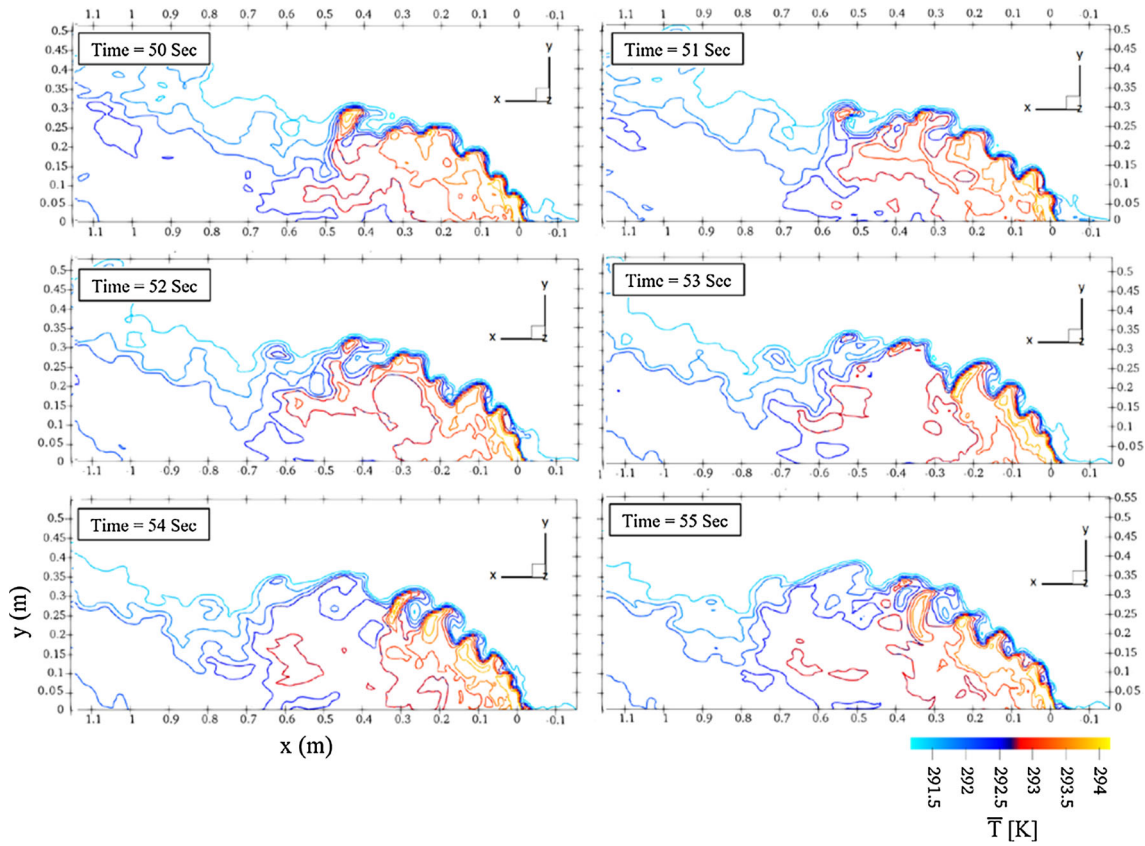


Fig. 17 The temporal evolution of the scalar temperature in planes located at $z = 12$ cm of 8E test

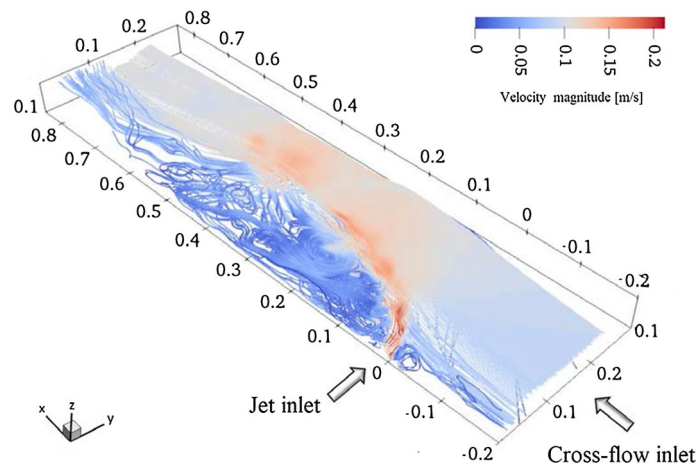


Fig. 18 The instantaneous streamline colored by the velocity magnitude of the 1E test

similar to tests with $R > 1$. The vortex shedding region is hardly determined in these cases. Also, the gradient of $(T_m)_{normalized}$ and $(U_m)_{normalized}$ profiles is not equal in any region.

The 1E test without the temperature difference between the jet discharged from the side channel and the cross-flow is numerically simulated, it is called 9E test. The maximum time-averaged velocity magnitude of the 1E test occurs at a farther distance from the inner wall than for the 9E test (Fig. 24).

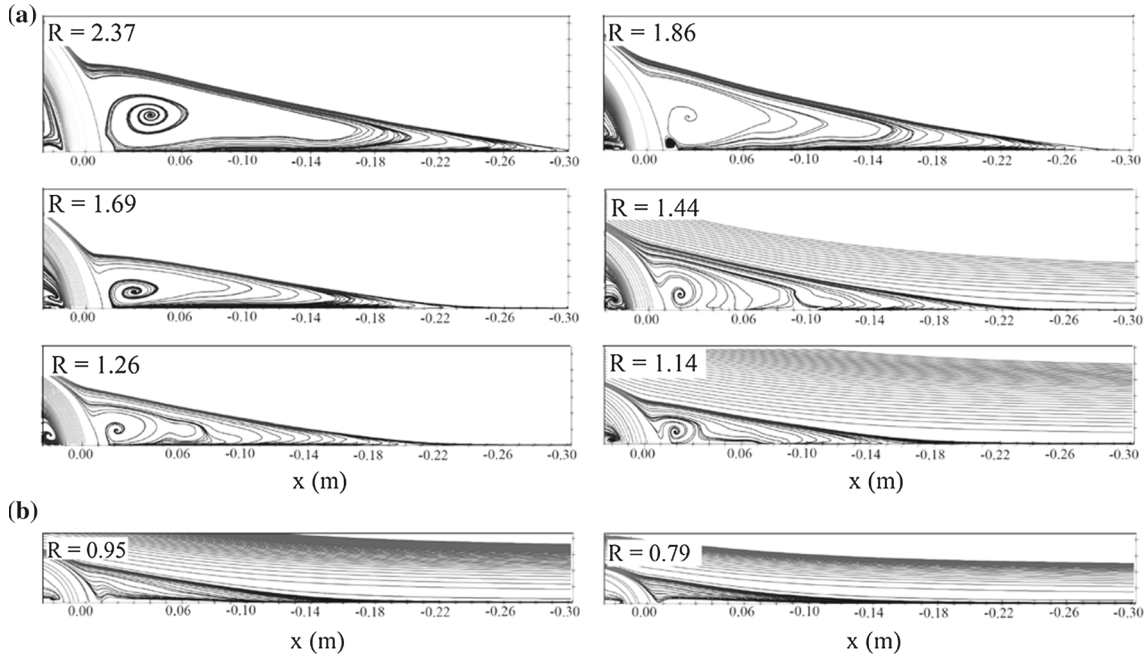


Fig. 19 The time-averaged streamline near the retardation area for a $R > 1$, and b $R < 1$

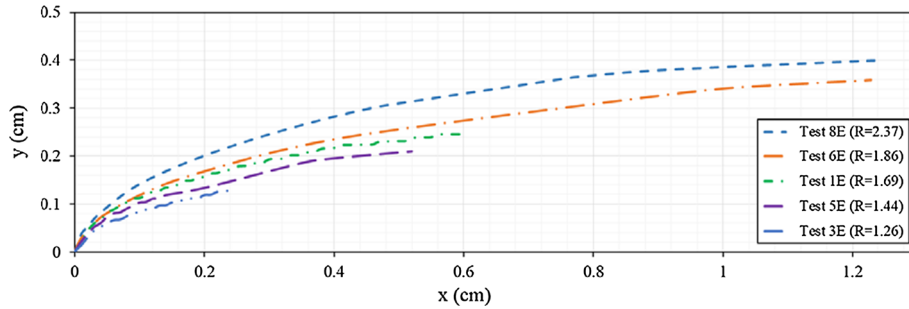


Fig. 20 The time-averaged trajectories of the surface buoyant jet in a plane located in $z = 12$ cm

4 Statistical analysis of the temperature mixing

The probability density function (PDF) is evaluated to investigate the mixing specifications at a determined location. The PDF at point x_I is defined as [31]:

$$f(\xi, x_I) = \{ \text{Probability of occurrence } \alpha_{I, KK} = \xi \}, \tag{18}$$

where α is the probability calculated by PDF, ξ is the statistical representation of α , x_I is the determined point (under investigation), and I is the spatial index, respectively. The mean (μ) and standard deviation (σ) of the discrete variable (ξ) with the probability function $f(\xi, x_I)$ are:

$$\mu = \sum \xi f(\xi, x_I), \tag{19}$$

$$\sigma = \sqrt{\sum f(\xi, x_I) (\xi - \mu)^2}. \tag{20}$$

Figure 25 shows the probability density of scalar temperature in different probes located at the following locations on the jet trajectory for the 1E test:

- Probe 01: ($x = 0.05, y = 0.08, z = 0.055$),
- Probe 02: ($x = 0.2, y = 0.16, z = 0.055$),

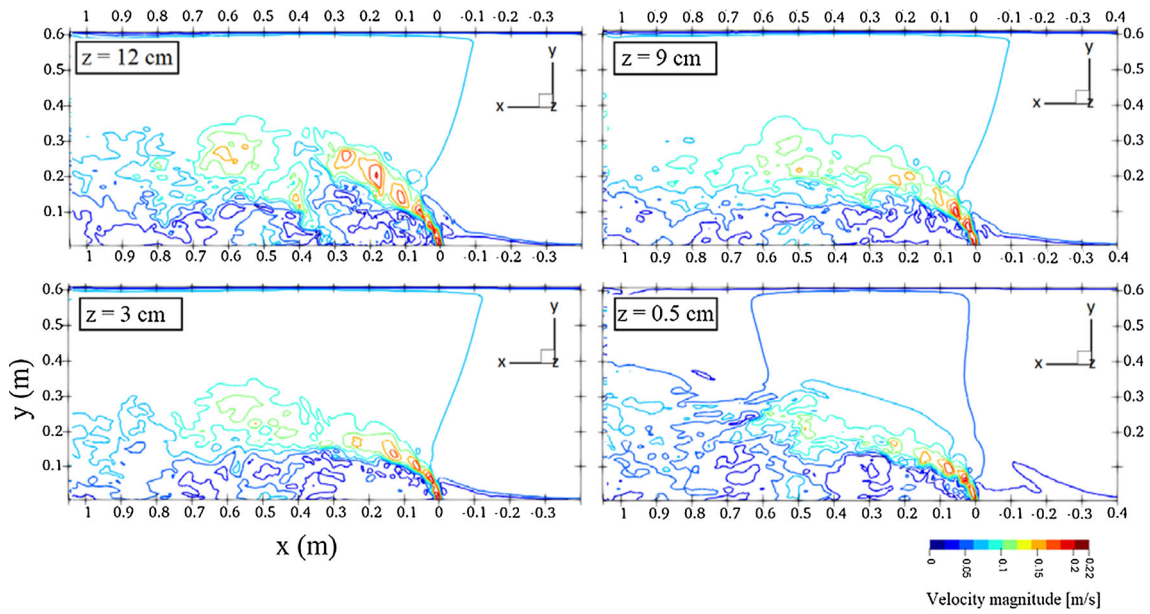


Fig. 21 Plan views of the instantaneous velocity magnitude at $z = 12, 9, 3,$ and 0.5 cm of the 8E test

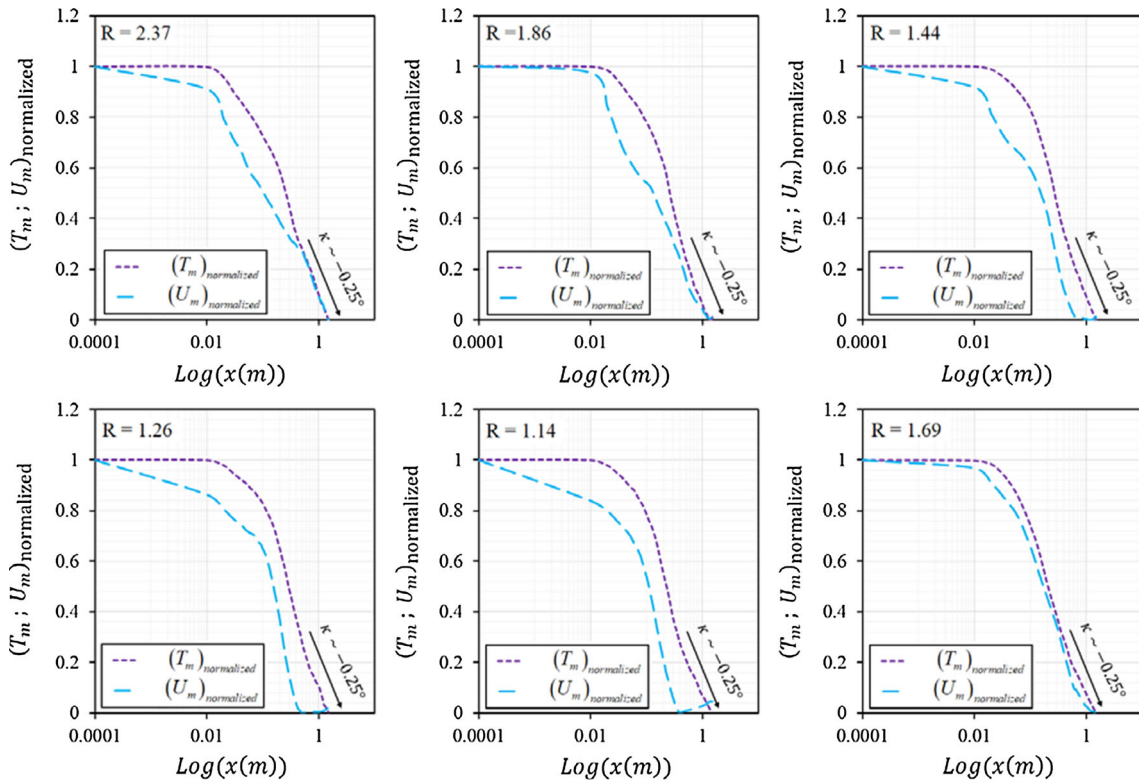


Fig. 22 The maximum time-averaged excess temperature and velocity magnitude normalized for tests with $R > 1$

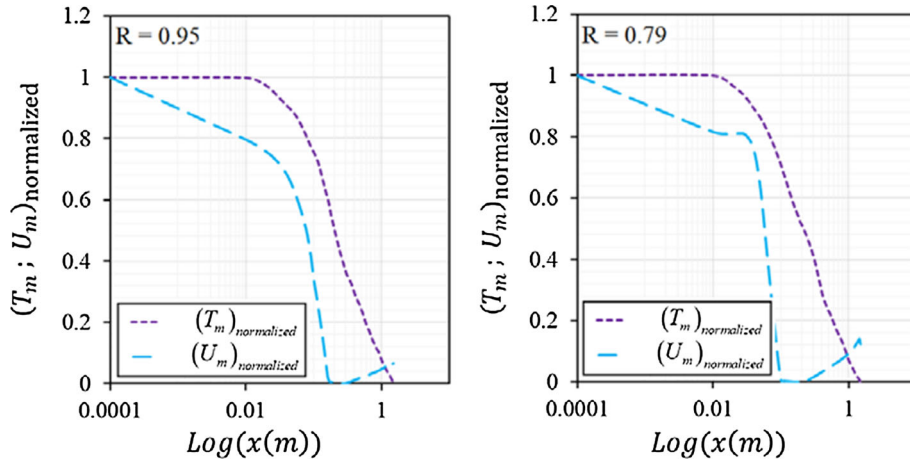


Fig. 23 The maximum time-averaged excess temperature and velocity magnitude normalized for tests with $R < 1$

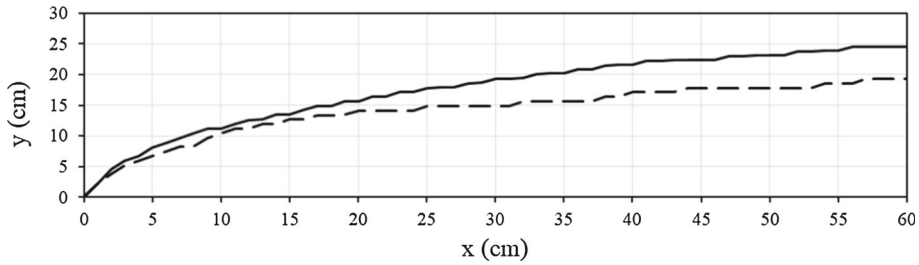


Fig. 24 The numerical simulation results of jet trajectory for the 1E test (solid line) and the 9E test (dashed line) at a distance of 0.5 cm under the free surface

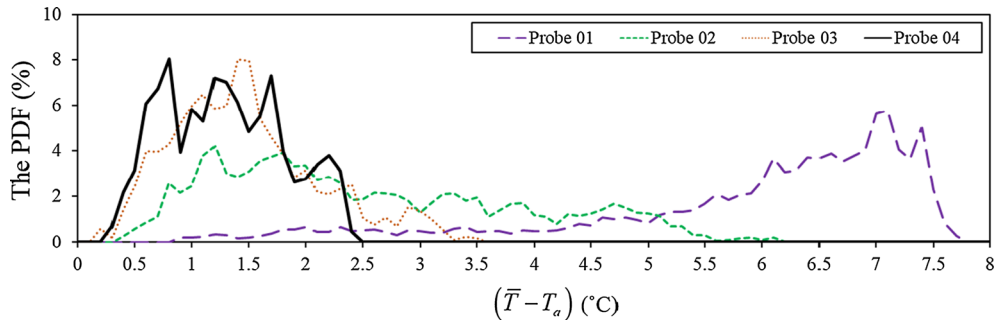


Fig. 25 The probability density of the excess temperature in the different locations of the flow field for the 1E test

Probe 03: ($x = 0.6, y = 0.245, z = 0.055$),
 Probe 04: ($x = 1.2, y = 0.29, z = 0.055$).

These locations cover the distance between the jet potential core and the far field of the buoyant jet. \bar{T} is recorded every 0.005 s during a period of 55 s (the experimentation period). The probability distribution in Probe 01 shows a significant left-skew with a mean of 5.85 and a standard deviation of 1.56. Due to the location of Probe 01 in the jet potential core, the peak of the graph is formed at high excess temperature values (Fig. 25). The probability distribution in Probe 02 illustrates the flattest profile in comparison with the probability distributions of the other locations and exhibits a stronger inhomogeneity due to the effects of the vortex shedding and unsteadiness in flow. And its PDF is scattered around its average value ($= 2.55$). The range of the excess temperature in Probe 03 is between 0.1 and 3.6, which covers nearly half of the excess temperature range. The PDF profile exhibits the most concentrated distribution in Probe 04 located at the downstream of the side-channel exit ($x = 1.2$ m) because of more homogeneous mixing in the far field (Fig. 25). This pattern has also been observed in other tests that are ignored here for brevity.

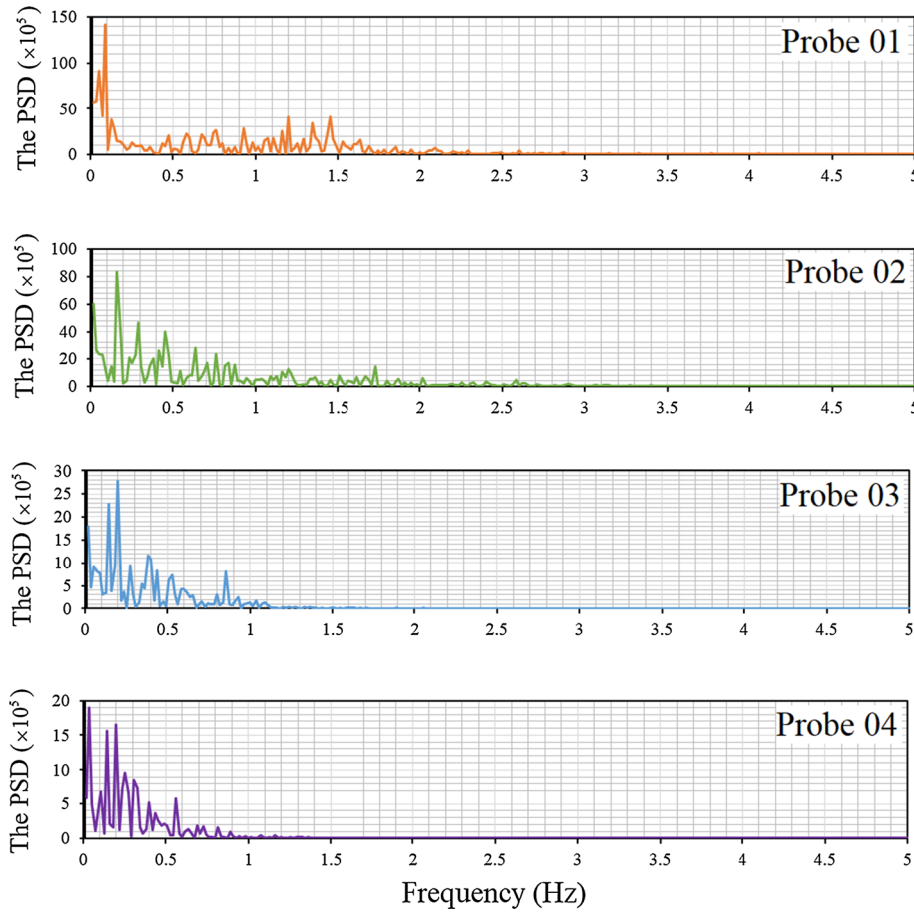


Fig. 26 The power spectral density of the temperature in different locations of the flow field

In order to describe the mixing characteristics of the discharged buoyant jet in the cross-flow, time series are studied through the power spectral density (PSD). The spectral analysis is applied to reveal the dominant frequencies and structures in the temperature fields. In our study, the PSD is generated by fast Fourier transformation (FFT) technique. Figure 26 shows the PSD of temperature in the probes. Similar to the PDF, all data are recorded every 0.005 s during a period of 55 s. This sampling method leads to captured signals with maximum frequency 100 Hz. A characteristic frequency of less than 20 Hz is observed for all probes. A dominant peak in the frequencies of 0.09 Hz and local peak in the range of 1 to 1.75 Hz occur in Probe 01. The local peak is observed only in jet potential core (Probe 01); it gradually disappears in the other probes by getting away from the side channel. The dominant frequency around the vortex shedding (Probe 02) is 0.16 Hz. Maximum peaks created PSD continuously reduced by getting away from the side channel. Two dominant frequencies 0.15 and 0.2 Hz are in Probe 03 and three dominant frequencies 0.036, 0.15, and 0.2 Hz are in Probe. The last two frequencies are equal to the dominant frequencies of Probe 03.

The temporal mixing deficiency (TMD) and spatial mixing deficiency (SMD) are calculated based on \bar{T} over the cross sections perpendicular to cross-flow at several locations ($0.05 < x < 1.2, 0.055 < z < 0.005, 0.00 < y < 0.61$). The SMD is a spatial heterogeneity measure of the time-averaged quantity in the flow field, whereas TMD is a temporal heterogeneity of the spatial average at various points over a plane. TMD and SMD at the point I over n snapshots are evaluated as [31]:

$$\text{TMD} = \text{Avg}_{\text{plane}} \left(\frac{\text{RMS}_I}{\langle T_I \rangle} \right), \tag{21}$$

$$\text{SMD} = \frac{\text{RMS}_{\text{plane}} (\langle T_I \rangle)}{\text{Avg}_{\text{plane}} (\langle T \rangle)}, \tag{22}$$

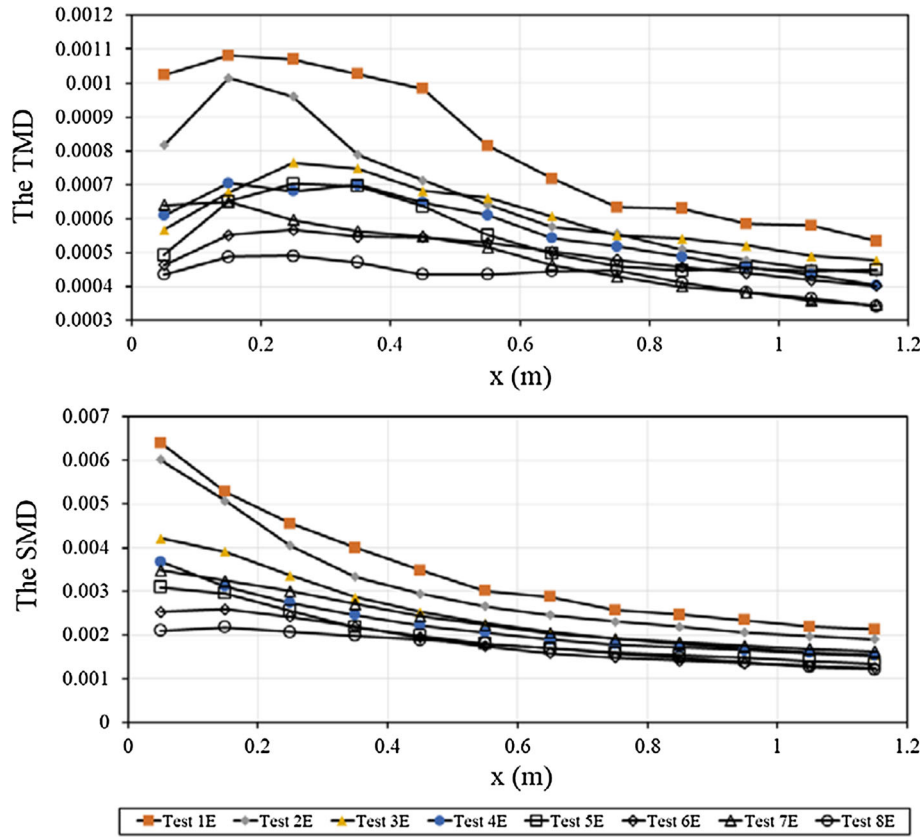


Fig. 27 TMD and SMD mixing indices

where

$$\langle T_I \rangle = \frac{1}{n} \sum_{KK=1}^n (\bar{T} - T_a)_{I, KK}, \quad (23)$$

$$\text{RMS}_I = \sqrt{\frac{1}{n-1} \sum_{KK=1}^n \left(\langle T_I \rangle - (\bar{T} - T_a)_{I, KK} \right)^2}, \quad (24)$$

$$\text{Avg}_{\text{plane}} (\langle T \rangle) = \frac{1}{m} \sum_{l=1}^m \langle T_l \rangle, \quad (25)$$

$$\text{RMS}_{\text{plane}} (\langle T_l \rangle) = \sqrt{\frac{1}{m-1} \sum_{l=1}^m \left(\langle T_l \rangle - \text{Avg}_{\text{plane}} (\langle T_l \rangle) \right)^2}, \quad (26)$$

where m is the number of nodes on each plane. Figure 27 shows the SMD and TMD calculated for 1-8E tests. \bar{T} is recorded every 0.04 s during a period of 55 s. Both indices are highest in the 1E test due to the most homogeneous mixing field. Conversely, both indexes are smallest in the 8E test, which denotes strongest inhomogeneity of the mixing field. TMD and SMD gradually decrease for all tests away from the side channel; it shows the inhomogeneity of the mixing field in the far fields. The maximum TMD occurs between $x = 15$ cm and $x = 25$ cm in the downstream of the side channel for all tests, which occurs around the vortex shedding region. There are also oscillatory behaviors in the profiles due to the effects of vortex shedding. Zhang and Yang [31] reported a similar trend of SMD and TMD for the transverse jet with a circular cross section discharged in the cross-flow. TMD and SMD increase by increasing the buoyancy flux (F_0).

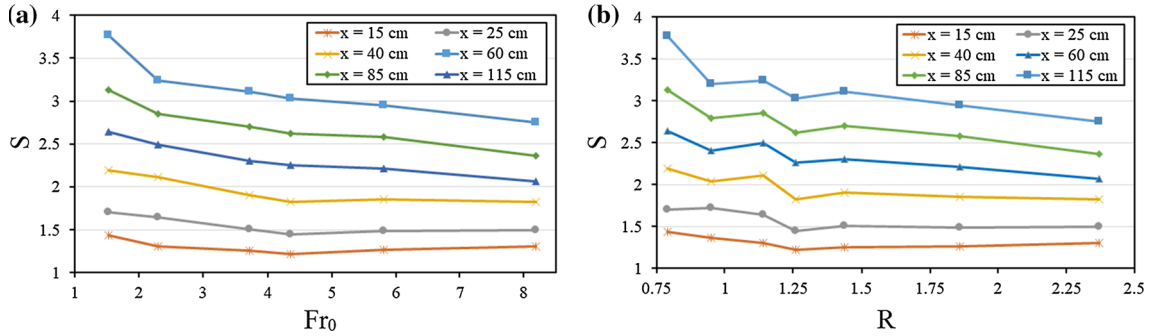


Fig. 28 The temperature dilution at different sections of the main channel: **a** densimetric Froude number and **b** the velocity ratio of the jet to the cross-flow

5 Parameter study

Fr_0 and R are utilized to describe the problems of discharged buoyant jets. Fr_0 is defined by Abdelwahed [8] as

$$Fr_0 = \frac{V_0}{\left(\frac{1}{\rho}g(\Delta\rho)\right)^{1/2} A_0^{1/4}} \tag{27}$$

The diluted parameter (S) which is defined by Yan and Mohammadian [29] is applied to study the Fr_0 and R effect on the mixing process of the buoyant jet and cross-flow:

$$S = \frac{T_0}{T_m - T_a} \tag{28}$$

Figure 28 indicates the Fr_0 and R effect on the temperature dilution in various cross sections. The temperature dilution generally decreases as Fr_0 and R increase. Also, it increase away from the discharge point due to the reduction in initial momentum. The temperature dilution variations are more significant at different cross sections for smaller Fr_0 and R .

6 Conclusion

In this paper, the detailed mixing characteristics and three-dimensional structure of the discharged water flow from a side channel in the cross-flow are investigated using the OpenFOAM model. The realizable $k-\epsilon$ turbulence model is applied to close URANS equations. The numerical simulation results are compared with the measured results of recirculation zone size, time-averaged excess temperature, half-width and half-thickness of the maximum time-averaged excess temperature, and jet trajectory at different cross sections of the main channel. The simulated results show a good agreement with experimental results.

The three-dimensional structure of instantaneous and time-averaged vortices and streamlines is examined for the different ratio of streamwise velocity in the side-channel inlet to the streamwise velocity in the cross-flow inlet (R). The line integral convolution (LIC) method is used to draw the streamlines. Besides, vortex structures are visualized by the Lambda-2 technique. A stagnated zone is formed in the confluence upstream. The turbulent motions can be observed in the recirculation zone structure. Near the discharge location, the flow is affected by the recirculation zone and a rotating vortex can be seen close to the wall involved the surface jet. Shear-layer vortices occur near the discharge location and at the confluence of the surface jet and cross-flow. Large-scale coherent structures are dominant near the discharge location, while the final structures are often smaller and more chaotic than the primary structures. The horseshoe and surface roller vortices occur at the discharge location upstream. Also, secondary vortices are in the far field and near the free surface. The vortices are concentrated near the free surface after the recirculation zone.

The temperature mixing is investigated using contours and slices. The instantaneous temperature contours near the free surface exhibit a vortex shedding phenomenon and gaps between the cross-flow and jet at the shear layer. The maximum time-averaged excess temperature and velocity magnitude profiles are examined to evaluate the link between the scalar mixing and flow dynamics. The maximum time-averaged velocity

magnitude profile immediately decreases with different slopes from the discharge location in the jet potential core. An irregularity is observed only for $R > 1$ in the maximum time-averaged velocity magnitude and excess temperature profile, especially in the velocity profile after the jet potential core. This region is the position where the surface jet sheds in the cross-flow. The decreasing slope of maximum time-averaged velocity magnitude and excess temperature profiles is almost constant in the far field from the side channel.

Mixing efficiency is quantified using the probability density function (PDF), power spectral density (PSD), temporal mixing deficiency (TMD), and spatial mixing deficiency (SMD). The PDF of the temperature shows a significant left-skew in the jet potential core. In the near field, there is a stronger inhomogeneity due to the effects of the vortex shedding and unsteadiness in the flow. The PDF exhibits a more concentrated distribution in the far field because of a more homogeneous mixing. According to the PSD, the characteristic frequency is less than 20 Hz in the flow field. Moreover, the maximum peaks which are created by the PSD are continuously reduced away from the side channel. TMD and SMD show a direct relationship between the mixing efficiency and buoyancy flux (F_0). In other words, TMD and SMD increase as F_0 increases. The temperature dilution generally increases with increasing Fr_0 and R .

References

1. Choi, K.-H., Young-Ok, K., Joon-Baek, L., Soon-Young, W., Man-Woo, L., Pyung-Gang, L., Dong-Sik, A., Jae-Sang, H., Ho-Young, S.: Thermal impacts of a coal power plant on the plankton in an open coastal water environment. *J. Mar. Sci. Technol.* **20**(2), 187–194 (2012)
2. Chuang, Y.-L., Hsiao-Hui, Y., Hsing-Juh, L.: Effects of a thermal discharge from a nuclear power plant on phytoplankton and periphyton in subtropical coastal waters. *J. Sea Res.* **61**(4), 197–205 (2009)
3. Constantinescu, G., Miyawaki, S., Rhoads, B., Sukhodolov, A., Kirkil, G.: Structure of turbulent flow at a river confluence with momentum and velocity ratios close to 1: insight provided by an eddy-resolving numerical simulation. *Water Resour. Res.* **47**(5), W05507 (2011)
4. Motz, L.H., Benedict, B.A.: Heated surface jet discharged into a flowing ambient stream. Report 4, Department of Environment and Water Resource Engineering, Vanderbilt University, Nashville, Tenn (1970)
5. Stolzenbach, K.D., Harleman, D.R.F.: An analytical and experimental investigation of surface discharges of heated water. Report 135, Ralph M. Parsons Laboratory for Water Resources and Hydrodynamics, Massachusetts Institute of Technology, Cambridge (1971)
6. Carter, H.H., Schiemer, E.W., Regier, R.: Buoyant surface jet discharging normal to an ambient flow of various depths. Technical report 81. No. COO-3062-13. Johns Hopkins Univ., Baltimore, Md. (USA). Chesapeake Bay Institute (1973)
7. Carter, H.H., Regier, R.: Three dimensional heated surface jet in a cross flow. Technical report 88. No. COO-3062-19. Johns Hopkins Univ., Baltimore, Md. (USA). Chesapeake Bay Institute (1974)
8. Abdelwahed, M.S.T.: Surface jets and surface plumes in cross-flows. Ph.D. thesis, Department of Civil Engineering and Applied Mechanics. McGill University, Montreal, Quebec (1981)
9. He, S., Xu, Z., Jackson, J.D.: An experimental investigation of buoyancy-opposed wall jet flow. *Int. J. Heat Fluid Flow* **23**(4), 487–496 (2002)
10. Abessi, O., Saeedi, M., Bleninger, T., Davidson, M.: Surface discharge of negatively buoyant effluent in unstratified stagnant water. *J. Hydro-environ. Res.* **6**(3), 181–193 (2012)
11. Teng, S., Feng, M., Chen, K., Wang, W., Zheng, B.: Effect of a lateral jet on the turbulent flow characteristics of an open channel flow with rigid vegetation. *Water* **10**(9), 1204 (2018)
12. Frigo, Arthur A., Frye, D.E.: Physical measurements of thermal discharges into Lake Michigan. No. ANL/ES-16. Argonne National Lab (1972)
13. Vaillancourt, G., Couture, R.: Influence of heat from the Gentilly nuclear power station on water temperature and Gastropoda. *Can. Water Resour. J.* **3**(3), 121–133 (1978)
14. Shah, V., Dekhatwala, A., Banerjee, J., Patra, A.K.: Analysis of dispersion of heated effluent from power plant: a case study. *Sādhanā* **42**(4), 557–574 (2017)
15. Roberts, P.J.W., Snyder, W.H., Baumgartner, D.J.: Ocean outfalls. I: submerged wastefield formation. *J. Hydraul. Eng.* **115**, 1–25 (1989a)
16. Roberts, P.J.W., Snyder, W.H., Baumgartner, D.J.: Ocean outfalls. II: spatial evolution of submerged wastefield. *J. Hydraul. Eng.* **115**(1), 26–48 (1989)
17. Roberts, P.J.W., Snyder, W.H., Baumgartner, D.J.: Ocean outfalls. III: effect of diffuser design on submerged wastefield. *J. Hydraul. Eng.* **115**(1), 49–70 (1989)
18. Jirka, G.H., Donker, R.L., Hinton, S.W.: User's manual for CORMIX: a hydrodynamic mixing zone model and decision support system for pollutant discharges into surface waters. US Environmental Protection Agency, Office of Science and Technology (1996)
19. Frick, W.E., Roberts, P.J.W., Davis, L.R., Keyes, J., Baumgartner, D.J., George, K.P.: Dilution models for effluent discharges. Visual Plumes, EPA/600/R-03 25 (2003)
20. Palomar, P., Lara, J.L., Losada, I.J.: Near field brine discharge modeling part 2: validation of commercial tools. *Desalination* **290**, 28–42 (2012)
21. Palomar, P., Lara, J.L., Losada, I.J., Rodrigo, M., Álvarez, A.: Near field brine discharge modelling part 1: analysis of commercial tools. *Desalination* **290**, 14–27 (2012)

22. Doneker, R.L., Ramachandran, A.S., Opila, F.: Multiport diffuser design for a negatively buoyant discharge. In: World Environmental and Water Resources Congress 2017, pp. 97–111 (2017)
23. Tang, H.S., Paik, J., Sotiropoulos, F., Khangaonkar, T.: Three-dimensional numerical modeling of initial mixing of thermal discharges at real-life configurations. *J. Hydraul. Eng.* **134**(9), 1210–1224 (2008)
24. Hwang, R.R., Yang, W.C., Chiang, T.P.: Effect of ambient stratification on buoyant jets in cross-flow. *Int. J. Multiph. Flow* **22**(S1), 125–126 (1996)
25. Yuan, L.L., Street, R.L.: Trajectory and entrainment of a round jet in crossflow. *Phys. Fluids* **10**(9), 2323–2335 (1998)
26. Valero, D., Bung, D.B.: Sensitivity of turbulent Schmidt number and turbulence model to simulations of jets in crossflow. *Environ. Model. Softw.* **82**, 218–228 (2016)
27. Muppidi, S., Mahesh, K.: Study of trajectories of jets in crossflow using direct numerical simulations. *J. Fluid Mech.* **530**, 81–100 (2005)
28. Paik, J.: Numerical simulation of thermal discharges in crossflow. In: 2011 IEEE 3rd International Conference on Communication Software and Networks (ICCSN), pp. 328–332. IEEE (2011)
29. Yan, X., Mohammadian, A.: Numerical modeling of vertical buoyant jets subjected to lateral confinement. *J. Hydraul. Eng.* **143**(7), 04017016 (2017)
30. Guan, H., Wu, C.J.: Large-eddy simulations and vortex structures of turbulent jets in crossflow. *Sci. China Ser. G* **50**(1), 118–132 (2007)
31. Zhang, L., Yang, V.: Flow dynamics and mixing of a transverse jet in crossflow-part I: steady crossflow. *J. Eng. Gas Turbines Power* **139**(8), 082601 (2017)
32. Xiao, J., Travis, J.R., Breitung, W.: Non-Boussinesq integral model for horizontal turbulent buoyant round jets. *Sci. Technol. Nucl. Install.* **2009**, 10 (2009)
33. Alfaihi, H., Mohammadian, A., Kheirkhah Gildeh, H.: Experimental and numerical study of thermal buoyant wall jet in calm ambient water. In: 22nd Canadian Hydrotechnical Conference, Montreal, Quebec, April 29–May 2 (2015)
34. Kheirkhah Gildeh, H., Mohammadian, A., Nistor, I., Qiblawey, H.: Numerical modeling of turbulent buoyant wall jets in stationary ambient water. *J. Hydraul. Eng.* **140**(6), 04014012 (2014)
35. Huai, W., Li, Z., Qian, Z., Zeng, Y., Han, J., Peng, W.: Numerical simulation of horizontal buoyant wall jet. *J. Hydrodyn.* **22**(1), 58–65 (2010)
36. McGuiirk, J.J., Rodi, W.: A depth-averaged mathematical model for the near field of side discharges into open-channel flow. *J. Fluid Mech.* **86**(4), 761–781 (1978)
37. McGuiirk, J.J., Rodi, W.: Mathematical modelling of three-dimensional heated surface jets. *J. Fluid Mech.* **95**(4), 609–633 (1979)
38. Wang, X., Cheng, L.: Three-dimensional simulation of a side discharge into a cross channel flow. *Comput. Fluids* **29**(4), 415–433 (2000)
39. Yu, L., Righetto, A.M.: Depth-averaged turbulence k– ω model and applications. *Adv. Eng. Softw.* **32**(5), 375–394 (2001)
40. Craft, T.J., Gerasimov, A.V., Iacovides, H., Kidger, J.W., Launder, B.E.: The negatively buoyant turbulent wall jet: performance of alternative options in RANS modelling. *Int. J. Heat Fluid Flow* **25**(5), 809–823 (2004)
41. Addad, Y., Benhamadouche, S., Laurence, D.: The negatively buoyant wall-jet: LES results. *Int. J. Heat Fluid Flow* **25**(5), 795–808 (2004)
42. Kim, D.G., Cho, H.Y.: Modeling the buoyant flow of heated water discharged from surface and submerged side outfalls in shallow and deep water with a cross flow. *Environ. Fluid Mech.* **6**(6), 501–518 (2006)
43. Peng, Y., Zhou, J.G., Burrows, R.: Modelling solute transport in shallow water with the lattice Boltzmann method. *Comput. Fluids* **50**(1), 181–188 (2011)
44. Tay, H.W., Bryan, K.R., de Lange, W.P., Pilditch, C.A.: The hydrodynamics of the southern basin of Tauranga Harbour. *NZ J. Mar. Freshw. Res.* **47**(2), 249–274 (2013)
45. Penna, N., De Marchis, M., Canelas, O.B., Napoli, E., Cardoso, A.H., Gaudio, R.: Effect of the junction angle on turbulent flow at a hydraulic confluence. *Water* **10**(4), 469 (2018)
46. Shih, T.-H., Liou, W.W., Shabbir, A., Yang, Z., Zhu, J.: A new k– ϵ eddy viscosity model for high Reynolds number turbulent flows. *Comput. Fluids* **24**(3), 227–238 (1995)
47. Frank, M., White, F.M., Corfield, I.: *Viscous Fluid Flow*, vol. 3. McGraw-Hill, New York (2006)
48. Oliveira, J., Raad, I., Issa, P.: An improved PISO algorithm for the computation of buoyancy-driven flows. *Numer. Heat Transf. Part B Fundam.* **40**(6), 473–493 (2001)
49. Miller, F.J., Poisson, A.: International one-atmosphere equation of state of seawater. *Deep Sea Res. Part A Oceanogr. Res. Pap.* **28**(6), 625–629 (1981)
50. Henkes, R.A.W.M., Van Der Vlugt, F.F., Hoogendoorn, C.J.: Natural-convection flow in a square cavity calculated with low-Reynolds-number turbulence models. *Int. J. Heat Mass Transf.* **34**(2), 377–388 (1991)
51. Jeong, J., Hussain, F.: On the identification of a vortex. *J. Fluid Mech.* **285**, 69–94 (1995)
52. Weber, L.J., Schumate, E.D., Mawer, N.: Experiments on flow at a 90° open-channel junction. *J. Hydraul. Eng.* **127**(5), 340–350 (2001)
53. Cabral, B., Leedom, L.C.: Imaging vector fields using line integral convolution. In: Proceedings of the 20th annual conference on Computer graphics and interactive techniques, pp. 263–270. ACM, (1993)
54. Webber, N.B., Greated, C.A.: An investigation of flow behaviour at the junction of rectangular channels. *Proc. Inst. Civ. Eng.* **34**(3), 321–334 (1966)
55. Shukry, A.: Flow around bends in an open flume. *Trans. ASCE* **115**, 751–779 (1950)
56. Best, James Leonard.: Flow dynamics and sediment transport at river channel confluences. PhD diss., Birkbeck (University of London), (1985)